The Upgraded Interaction Regions of HERA

M. Seidel

December 11, 2001

The HERA luminosity upgrade, scheduled to take place in 2001, presents a major modification of the machine. According to our experiences with the original design it is quite important to document every possible detail as well as numerical tools and procedures that have been used to design the interaction region (IR) layout. This report is intended to preserve such information for the future. We consider here the basic concept and choice of parameters, beam geometry and optics, electron/positron switching, particle background, synchrotron radiation, orbit correction, tables with magnet positions and all relevant parameters along the beamlines to about 65 m. Furthermore a brief description of the geometry code that has been developed specifically for the HERA interaction region, will be given.

1 Concept and Parameters

Since the philosophy of the HERA upgrade has been discussed extensively somewhere else [1] [2] we will review here only the basic parameters. The concept foresees an early separation of the two beams, close to the interaction point (IP), with superconducting combined function magnets that are installed inside the experimental detectors. This allows to move the proton final focus magnets from 26 m distance to the IP in the original design, to 11 m. This in turn results in the possibility to focus the beam stronger and to achieve a spot size of $120 \times 30\,\mu\mathrm{m}^2$. The spot size of the electrons is matched to the same values by reducing both, the IP β-functions as well as the beam emittance. The combination of emittance and β-function is chosen such as to reach a beam-beam tuneshift of $\Delta\nu_y^e = 0.04$, which we consider as the possible limit for the electrons.

	e-Beam	p-Beam
energy [GeV]	27.5	920
beam current [mA]	58	140
emittance [nm]	22	$5000/\gamma$
emittance ratio $\varepsilon_y/\varepsilon_x$	0.18	1
rms bunch length [mm]	12	128
beta-functions β_x^*, β_y^* [m]	0.63, 0.26	2.45, 0.18
spot size $\sigma_x \times \sigma_y$ [$\mu\mathrm{m}^2$]	118×32	118×32
bb tune shift/IP $\Delta\nu_{x,y}$	0.027, 0.041	0.002, 0.0005
minimum aperture [σ]	20	12
Luminosity	$7.00 \cdot 10^{31}\mathrm{cm}^{-2}\mathrm{s}^{-1}$	

Table 1: Start-up parameters for the HERA upgrade.

To realize the new concept, the whole IR, up to about 65 m distance from the interaction

point, has to be modified. New magnets were designed and manufactured. The design of each magnet has been adopted to the special requirements at its location, as for example beam envelopes, the distance to the other beam, or the need to safely handle synchrotron radiation (SR). The superconducting magnets have large apertures to allow the passage of SR, and at the same time relatively small outer diameters to fit them into the experimental detectors. The electron final focus magnets, named GI and GJ, have gaps between the coils for passage of SR and for installation of NEG pumps. They are followed by the first exclusive proton quadrupole magnets, two GM's, which are half quadrupoles with mirror plates to allow close passage of the electron beam. The next quadrupoles of type GN and GA have a hole between the coils and the return yoke for the electron beam, and the GN's exhibit additionally a gap between the coils for the SR fan.

2 Interaction Region Lattice

2.1 Focusing Scheme

The focusing scheme is different for both beams. The electrons or positrons are focused by a triplet structure that consists of three single quadrupoles. On the left side the first quadrupole is the superconducting GO, followed by a GI and a GJ. On the right side the quadrupole component of the superconducting GG quadrupole is set to zero and the triplet structure is made up of two GI's and one GJ. Nevertheless it would be possible to use the GG as an additional degree of freedom, if required in the future.

Following an original proposal by B. Parker the protons are focused by a double doublet structure, i.e. four lenses. Although, in principle one could also use a single doublet, this scheme was chosen to limit the peak β-functions. Because of the high beam energy each lens has to be made up of several quadrupoles. In total the double doublet consists of 13 magnets, most of them more than 3 m long. The proton beam optics is of course affected also by the electron triplet since both beams have to pass it. Here the positron operation is the more difficult case since the triplet weakens the action of the GM half quadrupoles. At 920 GeV most of the magnets reach the limit of their focusing strength. A further raise of the energy would only be possible in a different focusing scheme, with consequently much smaller luminosity. Since practically all available space aside the IR is filled with quadrupoles we have a rather big flexibility to apply a different focusing scheme by electrically reconnecting the magnets.

The β-functions for both focusing schemes are shown in Fig. 1. For protons the peak β functions are about 1400 m vertically and 1750 m horizontally. This has to be compared with average β-functions in the arc of about 80 m in both planes.

The optics of the complete machines were worked out by B. Holzer for the protons [3], and E. Gianfelice, G. Hoffstätter for the electron machine [4]. The new electron machine lattice involves also the reduction of the beam emittance by stronger focusing. The phase advance per cell will be increased from presently 60° to 72°. A specific problem of the electron machine is beam polarization, which is an important part of the HERA physics program. In the course of the upgrade solenoid compensation coils will be removed from the detectors. At the same time longitudinal spin rotators will be installed also in the IR's south and north. With longitudinal polarization it is in principle possible to pass the detector solenoid without affecting the spin orientation. However, since the bending field of the sc. separation magnets is overlaid with the solenoid field, the beam trajectory is not exactly straight. This effect has to be compensated with correction coils on the sc. magnets. Furthermore the coupling introduced by the solenoid has to be corrected non-locally with tilted quadrupoles. These problems are being investigated

	electrons/positrons	protons
location	behind QLR67	behind BTR57
z	$67.600\,\mathrm{m}$	$57.213\,\mathrm{m}$
x	$-0.5155\,\mathrm{m}$	$0.0158\,\mathrm{m}$
x'	$-0.01\,\mathrm{rad}$	$0\,\mathrm{rad}$
y	$0\,\mathrm{m}$	$0\,\mathrm{m}$
y'	$0\,\mathrm{rad}$	$0\,\mathrm{rad}$

Table 2: Orbit conditions that have to be matched in order to connect the new IR geometry to the existing orbit in the arcs (left side symmetric). The z-axis is a tangent to the electron beam in the IP, x is the horizontal and y the vertical distance of the beam to this axis.

by M. Berglund [5].

2.2 Geometry for Protons on Electrons

Design criteria for the beam orbit (design trajectory) are the boundary conditions given by the magnet shapes and the available apertures. For the electron beam we have to consider also the shape and the direction of the SR-fan, as well as off-momentum particle loss due to dispersion orbit.

The deflection angles of the superconducting magnets are chosen such that electron beam and proton beam have the minimum required separation at the septum quadrupoles of type GM which focus the protons. On the left side the superconducting magnet GO deflects the electron beam to 8.21 mrad, and the first offset GI quadrupole back to 7.2 mrad, GJ to a larger angle of 8.0 mrad and the small dipole BO to the final separation angle of 8.6 mrad which is kept then up to 41 m. The quadrupoles produce relatively wide synchrotron radiation fans since the beam tails experience high fields. The scheme to deflect back and fourth in the quadrupoles has been chosen to tilt the radiation fan from GJ, which is further away from the IP than GI, such that it moves into the GI fan. Furthermore this arrangement reduces the radiation from the beam tails in these quadrupoles (see the section on SR for more details). For symmetry reasons the right side is made similar, however, the final separation angle is here slightly larger, 8.8 mrad. At larger distance from the IP we introduced a dispersive magnet structure ("dogleg"), to allow for momentum collimation (see section below). The beam angles as a function of distance to the IP are shown in Fig. 2.

To match the geometry to the existing machine the conditions listed in table 2 have to be met. In case of the protons these conditions are obtained by varying the strengths of the dipoles BQ and BW, for the electrons BN and BH, the dogleg magnets. Note that the proton BP dipoles have the same set values in order to save an expensive powersupply.

The layout of the vacuum system has been made such that the minimal aperture for the electron beam is nominally $20\,\sigma$ and $12\,\sigma$ for the protons. This rule is slightly violated at one tight spot on the left side around BQ/GN, where the electron aperture is reduced to $19.5\,\sigma$. The tightest apertures occur for the electrons in the mentioned BQ/GN location and for the protons in the second (away from IP) half quadrupole GM. A schematic layout of the interaction region is shown in Fig. 3.
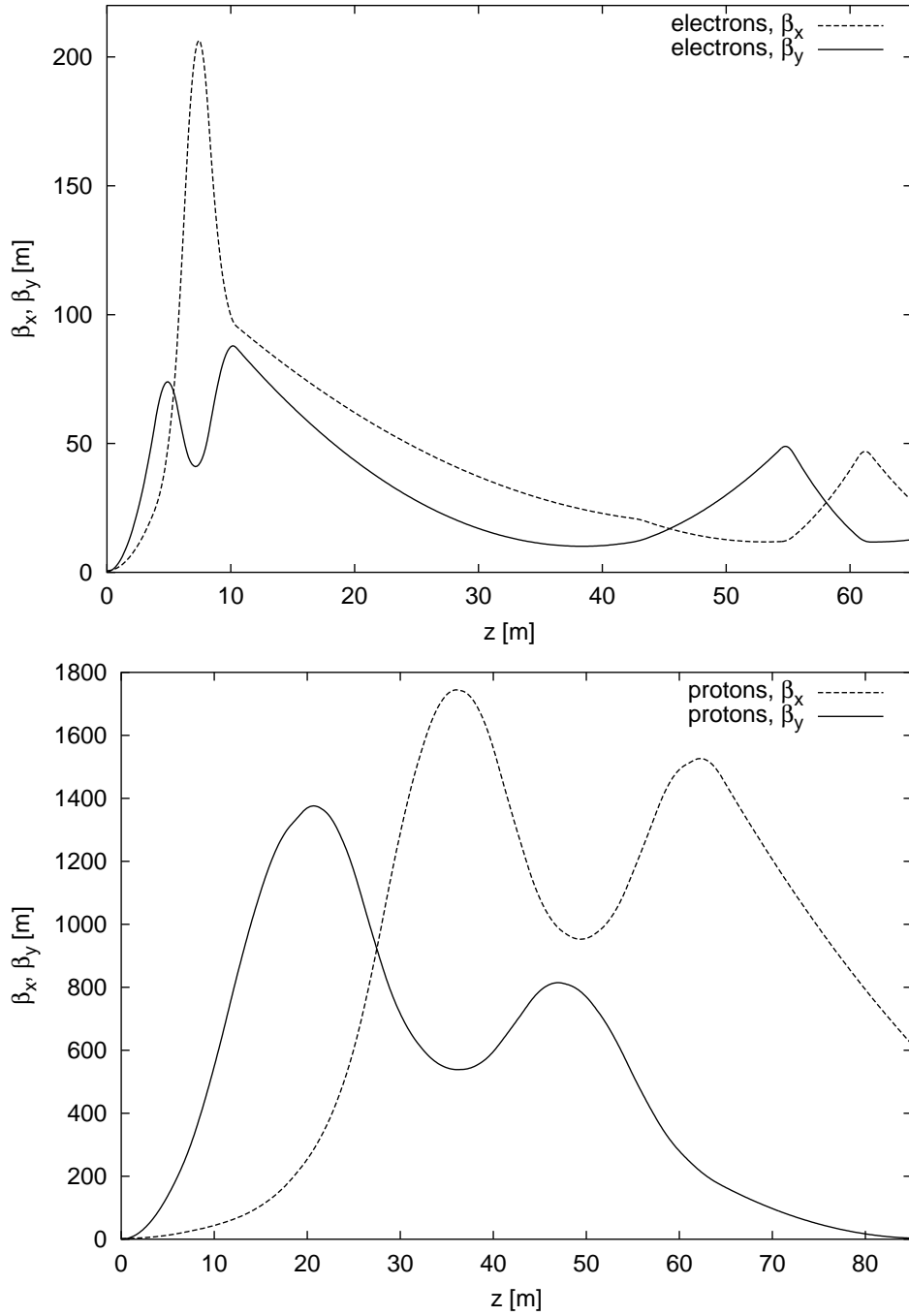
Figure 1: Beta-functions for both beams in the vicinity of the IR (which is located at $z = 0$), demonstrating triplet focusing for the electrons (upper) and double doublet focusing for the protons.
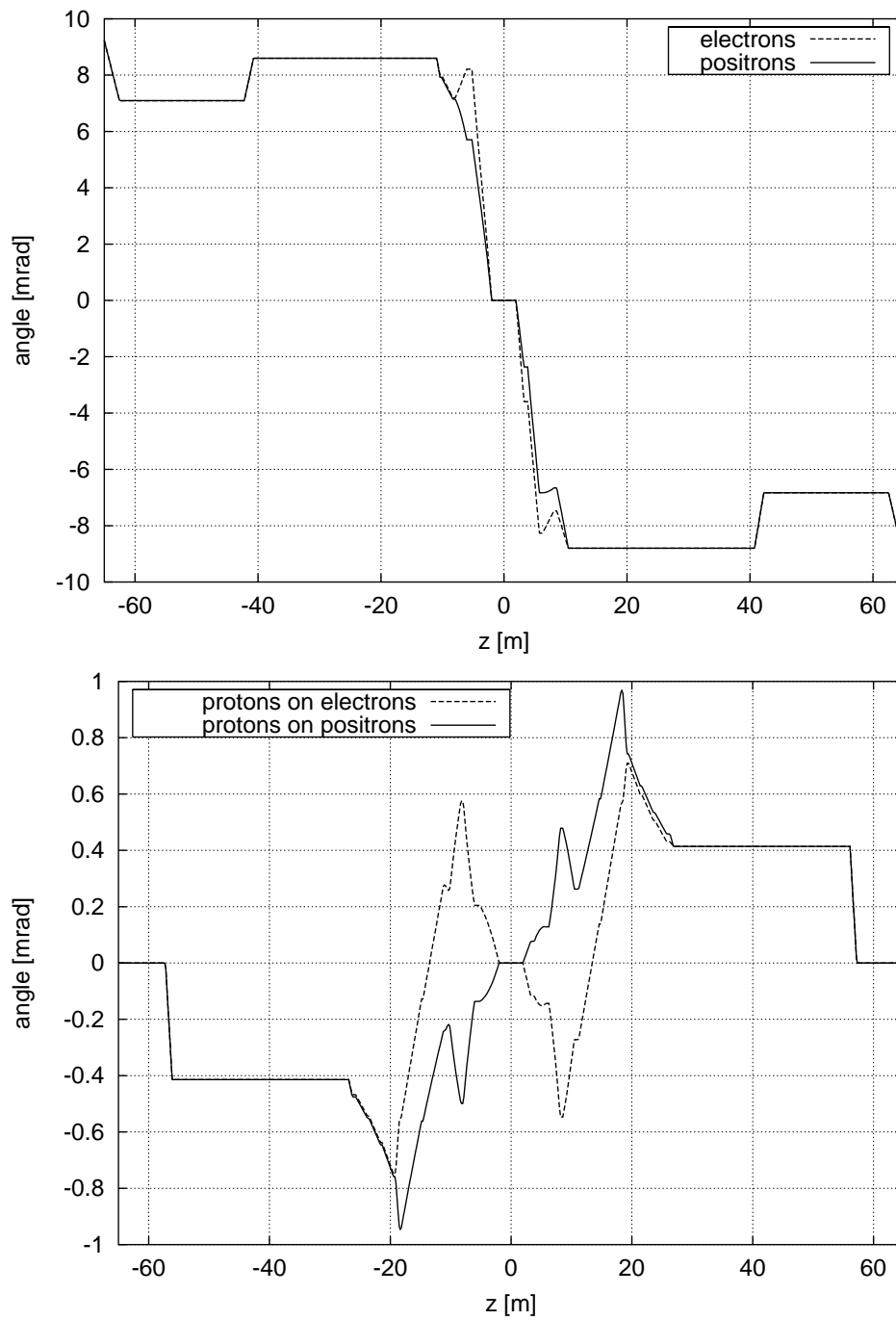
Figure 2: Angles of the electron/positron beam (upper), and the proton beam vs. detector axis as a function of the distance to the IP.
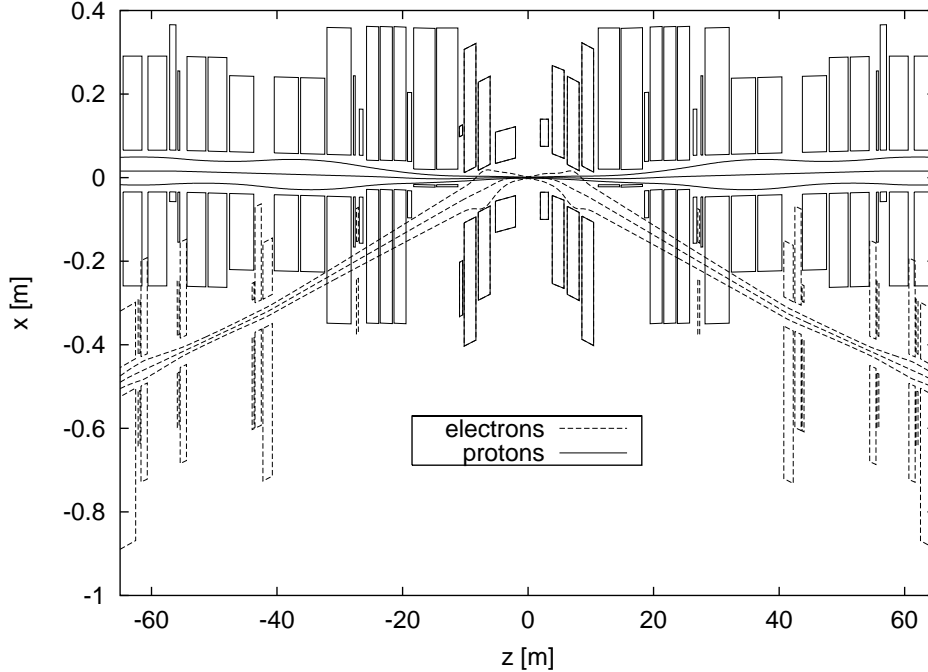
Figure 3: Layout of the interaction region, the part to be modified, for electron operation.

2.3 Switching to Positron/Proton Operation

In order to collide positrons with protons the polarity of the electron magnets has to be switched. Since the proton beam does not change the sign of its charge, it will be deflected with different polarity as compared to the electron case. Because of the high proton energy the difference angle is not big, but it has to be corrected. A convenient solution would be an additional dipole magnet, however, at the expense of luminosity because the dipole would increase the distance from the IP to the proton final focus magnets. We aim for the maximum luminosity and adopted a different solution, proposed by F. Willeke, that foresees to move the IP transversally by 7.5 mm inwards for positron operation. The proton beam starting from this coordinate crosses the proton beam for electron operation just at the end of the second GM, which is the point with the tightest aperture in the machine. Behind this quadrupole we install a small septum like dipole (BQ) to correct the remaining angle, such that both beams have roughly identical orbits beyond that magnet. All proton magnets can stay in place. The positron orbit is adjusted to match the electron orbit by small transverse position changes of the electron final focus magnets of type GI and GJ (see Fig. 4). In total 5 magnets have to be moved up to 7 mm, which is possible without changing vacuum components. A special situation arises at H1. The detector solenoid field applies a relatively large force on the end fields of the sc. dipole magnet GO. At H1 this magnet is mounted to the liquid argon cryostat of the detector, which is not a very rigid support. In order to reduce the force on the magnet it will be shifted transversally by 4.4 mm as compared to the ZEUS arrangement, but only for the electron case. This shift reduces the field from the dipole coil since the quadrupole overtakes some of its action. The settings of the GO are listed for the individual cases in table 3 and are also shown with the beam orbit in Fig. 5.

6

	Dipole Part of Field [T]	Magnet Offset vs. Detector Axis at IP End [mm]	hor. tilt angle wrt. detector axis [mrad]
H1/e^+	0.092	+2.0	4.1
H1/e^-	0.180	+6.4	4.1
ZEUS/e^+	0.092	+2.0	4.1
ZEUS/e^-	0.237	+2.0	4.1

Table 3: Settings for the GO sc. magnet at both experiments for both lepton species.
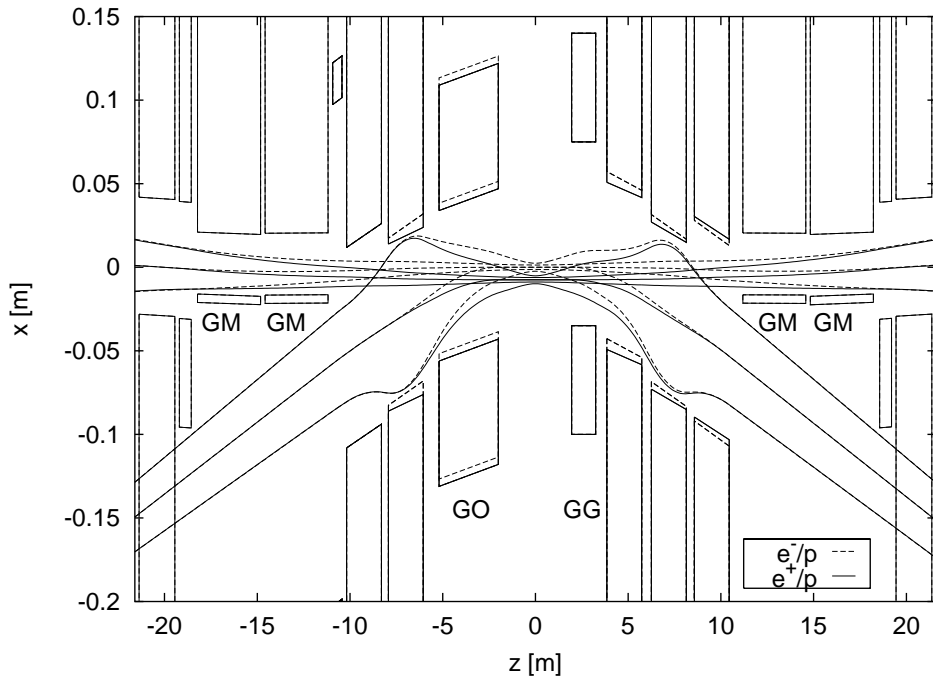
Figure 4: Layout of the interaction region showing differences for electron or positron operation (here: H1 with GO moving, solid lines: e^+ beam envelopes and corresponding magnet positions, dashed: e^- case).
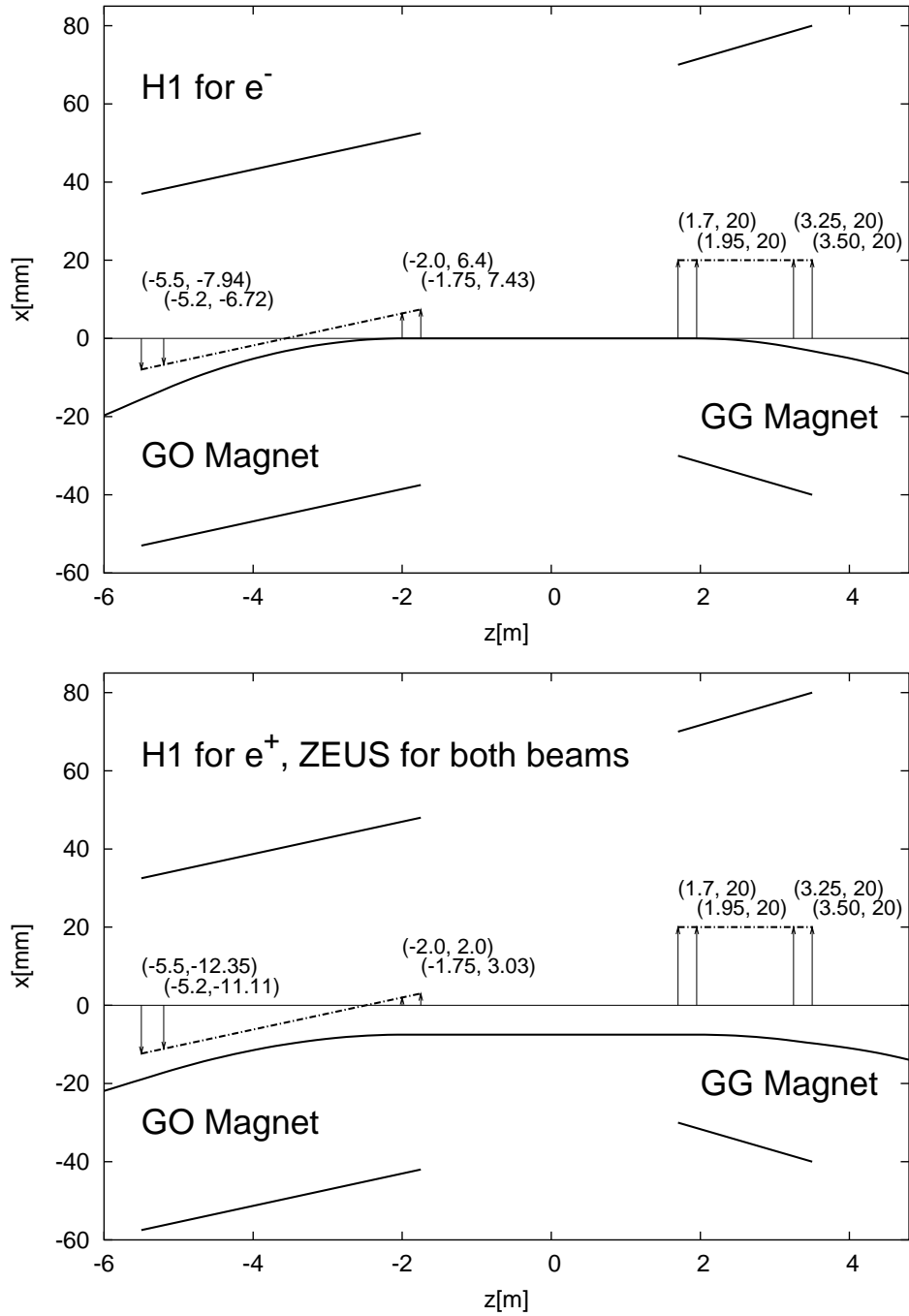
Figure 5: Arrangement of the sc. magnets for the individual cases in top-view. The dash-dotted line represents the magnet axis, the thick black lines the magnet apertures. The numbers in brackets are the magnet axis coordinates for the mechanical ends of the magnets, as well as the start and end points of the fields (indicated by arrows). Furthermore the lepton beam orbits are indicated.

Figure 6: Proton injection beam $(6.5\,\sigma)$ in comparison with proton luminosity beam $(12\,\sigma)$.

2.4 Proton Beam Injection Optics

At the injection energy of $40\,\text{GeV}$ the beam exhibits an emittance which is 23 times bigger than at $920\,\text{GeV}$. Consequently it is impossible to fit the $12\,\sigma$ envelope through the aperture. However, according to our experience in the past, a minimum aperture of $6.5\,\sigma$ is en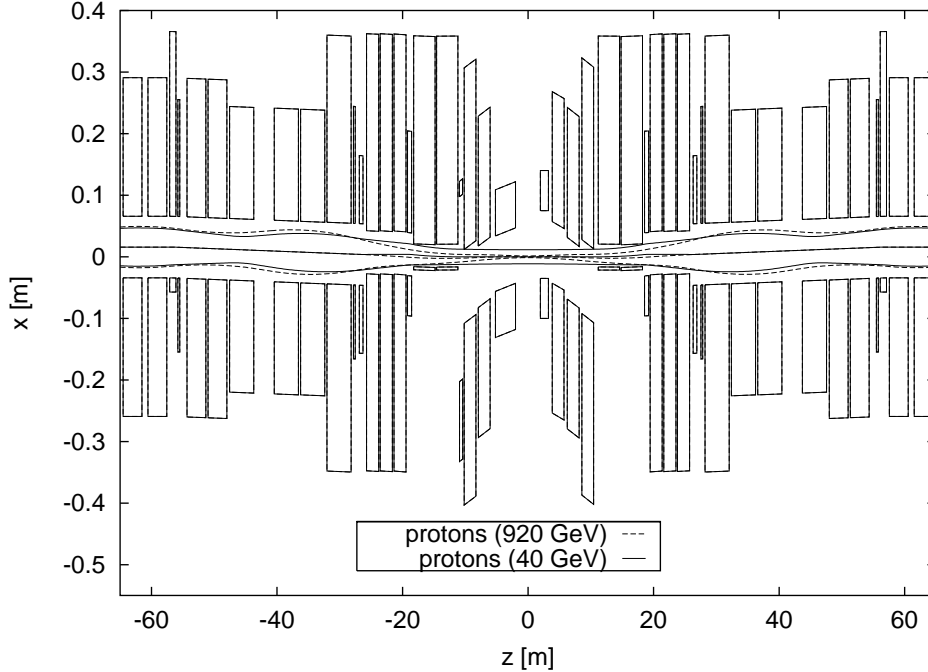ough for a limited storage time at injection energy, and furthermore the β-function at the IP can be relaxed. At proton injection conditions we assume that the electron magnets are switched off. Therefore it is not necessary to distinguish electron and positron operation. The geometry has been matched such as to fit the tightest aperture spot in the second GM magnet. To achieve this the beam has to pass the IP at $x = 0\,\text{mm}$. The beam envelopes are shown in Fig. 6. Furthermore the required "stay-clear" ellipses are shown for the proton beam at $920\,\text{GeV}$ and $40\,\text{GeV}$ in Fig. 7.

3 Particle Background

The major qualitative change in the IR layout is the early beam separation in the detectors, very close to the IP's. Electrons that have lost energy due to beam gas interactions upstream of the IR will preferentially hit the detector beampipe because they receive a larger deflection angle by the separation fields.

One can expect that the detector background caused by such losses will be increased by a large factor as compared to the present situation since the separating fields occur now inside the detector. In order to relax this problem we have foreseen to install a dispersive magnet structure, called "dogleg", in the straight section upstream of the detector, and for symmetry reasons also downstream. The dogleg contains two dipole magnets, BH and BN, that deflect the beam back and forth. Dispersion functions for off-energy particles produced in different regions are shown in Fig. 8. Those dispersion functions are computed by tracking an off energy beam through the lattice with magnets fixed in position, i.e. they include all nonlinear effects.
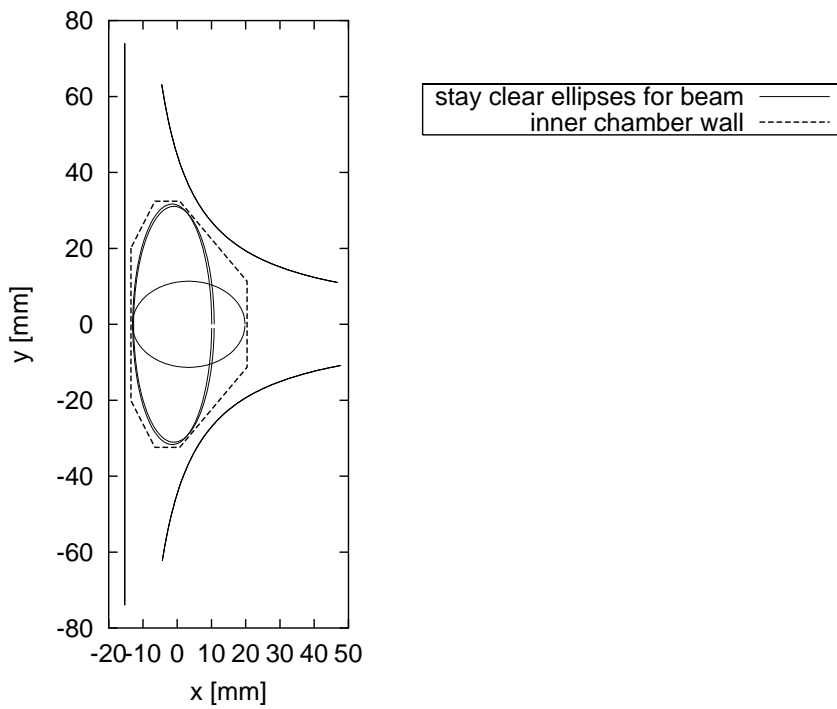
9

Figure 7: The two proton luminosity beams ($12\,\sigma$, upright ellipses), and the proton injection beam ($6.5\,\sigma$) at the tightest aperture spot, the end of the second GM type half quadrupole. The magnet poles are qualitatively indicated on the right side, the magnet mirror plate on the left side. The dashed line represents the inner boundary of the vacuum chamber.
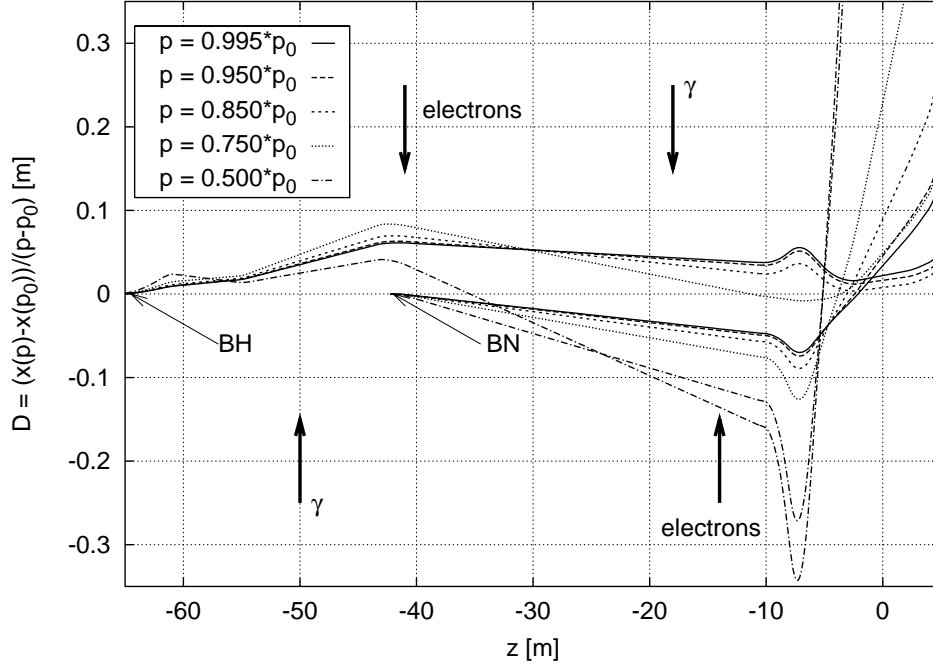
Figure 8: Beam dispersion for particles that undergo bremsstrahlung events upstream of BH and upstream of BN.

Collimators are installed at about $-41\,\mathrm{m}$ to capture electrons that lost energy upstream of BH, and at $-14\,\mathrm{m}$ for the ones produced inbetween the dogleg magnets. These magnets produce synchrotron radiation which also has to be collimated. The γ collimators are located at about $-50\,\mathrm{m}$ and $-18\,\mathrm{m}$. SR background in the ZEUS IR has been investigated by E. Lohrmann [6]. The locations of all four collimators are indicated in Fig. 8.

Tracking simulations were performed by U. Kötz [7]. Based on a uniformly distributed residual gas pressure profile across the IR, $P = 5 \cdot 10^{-9}\,\mathrm{mbar}$, Bremsstrahlung-events between electrons and gas molecules were simulated. The electrons that lost energy were tracked through the lattice into the detector. If the particles hit the detector beam pipe, the particle energy and the z-location where the beam gas interaction occurred are registered. Fig. 9 shows typical results of such simulations. The upper plot shows the simulation without the dogleg (dipoles are switched off, beamline is assumed to be straight), and the lower one with it. The electron collimators at $-40\,\mathrm{m}$ and $-14.6\,\mathrm{m}$ are positioned at $-25\,\sigma_x$ and $+8.6\,\sigma_x$ respectively. One can see that all particles produced beyond the first dogleg magnet, at about $60\,\mathrm{m}$, are effectively removed. Some of those that are produced inbetween the two magnets can still make it to the detector. The rate of these electrons is connected to the setting of the $14\,\mathrm{m}$ collimator. The $8.6\,\sigma_x$, chosen in the simulation is already very tight.

On the other hand we expect the vacuum conditions in the cavity section beyond $80\,\mathrm{m}$ to be especially bad, a fact that has been disregarded in the simulation. So one can consider the main purpose of the dogleg to remove electrons from the beam that interact in this region, and this seems to work well.
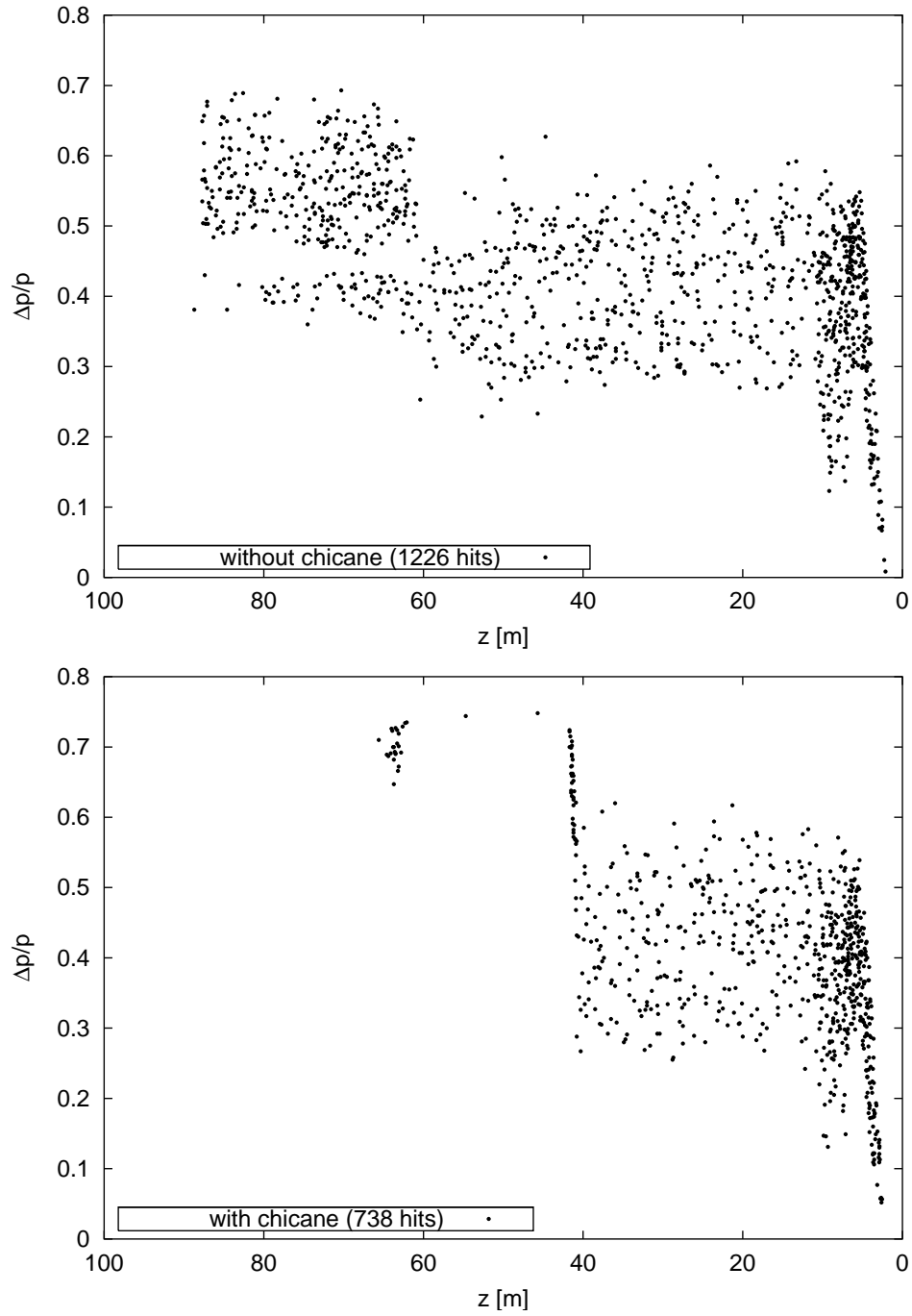
11

Figure 9: Result of a tracking simulation showing electrons that hit the detector beam-pipe. The fractional energy of the electron is plotted against the z-location where it lost energy due to bremsstrahlung with a residual gas molecule. Both plots present a comparison of the situation without (upper) and with chicane (courtesy U. Kötz, details see text).

4   Synchrotron Radiation

Another implication of the early beam separation concept is the production of SR *inside* the detector. The radiation cannot be collimated upstream of the detector, as it is realized in the present layout. This means that geometry and apertures have to be arranged such that the SR fan passes the detector with very small losses ($< 10^{-8}$). In order to predict the losses we needed an accurate procedure to compute the spatial radiation distribution from the beam. Such codes have been developed by both experiments and the machine group. Though the underlying strategies (tracking vs. semianalytic approach) are rather different, the results are in satisfactory agreement. Details of the numerical algorithm used here are described in the Appendix. Downstream of the detector the radiation is transported relatively far from the detector, collimated at 11 m for splitting of the beam pipes [8], and finally absorbed at 26 m. All simulations are done for a beam energy of 30 GeV.

4.1   SR Basics

The total radiation power from a Gaussian beam in a slice of a combined function magnet is:

$$\frac{dP}{dl} = 14.097 \cdot IE^4 \left[\frac{1}{\rho^2} + K^2(\beta_x \varepsilon_x + \beta_y \varepsilon_y) \right] \tag{1}$$

The result is obtained in kW/m for the current I in A, beam energy E in GeV, bend radius ρ in m and k-value K in m^{-2}. With HERA emittance and β functions (in m) the quadrupole term contribution is typically in the % range of the dipole term contribution. The main part of the power is produced in the sc. separation magnets and the first GI quadrupole on the right side. Since the electrons are deflected back and forth (see Fig. 2) they radiate about 10 kW more power than the positrons. Another characteristic property of the radiation is the spectral distribution of the photons. Typical critical energies are 150 keV. This is significantly higher than in the old design and radiation damage of beamline components is a point of concern.

$$E_c = 2.218 \, \frac{E^3}{\rho} \tag{2}$$

Here the result is obtained in units of keV. Figs. 10 and 11 show radiation power and critical energies along the IR beamline.

4.2   Distribution of Projected Radiation Patterns

The distribution of the radiation fan is of interest for the experiments because of background reasons, and for the layout of the vacuum system to estimate cooling requirements. The power densities that are under investigation for these two points of concern are very different though. The detectors desire a suppression ratio of $10^{-10} \ldots 10^{-8}$ for the radiation falling on the detector pipe, compared to the maximum density in the fan, whereas for absorbers and beam pipes the heat load, i.e. kW-powers are of interest. With the semianalytic approach, described in the Appendix, we are able to make precise computations of SR projections, however, always under the assumption of a Gaussian particle beam distribution. As is commonly known the particle beam can have Non-Gaussian tails, especially at large amplitudes. In principle the beam tails can be tested with scraper experiments down to relatively low densities of the order of 10^{-8}. Beyond that it seems very difficult to determine particle densities. Therefore the very low SR power densities that are shown in the plots below have to be considered as optimistic estimates.
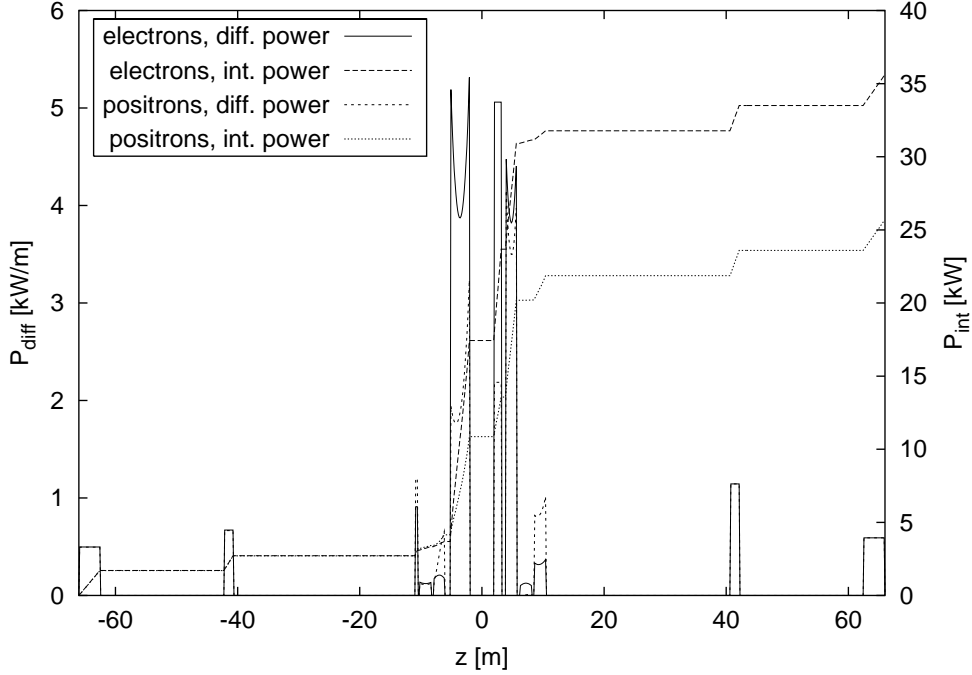
Figure 10: Differential SR power (power per unit length) and integrated power for electron and positron beam with design parameters over the IR section.

Another important question is how the radiation fan changes in case of misaligned magnets or a mis-steered beam. From such computations one can derive the allowed positioning tolerances of beam pipes and absorbers. Furthermore we are planning to install photoelectric SR detectors to monitor the position of the radiation fan. Here one would like to know which information on the beam orbit one can get at certain detector positions.

In Fig. 12 we show examples for one-dimensional radiation profiles in the close vicinity of the IP. Fig. 13 shows a two-dimensional profile at about 24 m on the right side. At this location it is planned to install radiation detectors for probing the vertical position of the fan. In the lower plot the profile is shown for a vertically misaligned beam. The radiation spot on the outer (right) side becomes higher. It is produced by the electron final focus magnets on the left side of the IP. Those magnets are more or less in line and the misaligned beam performs an oscillation while passing through them. This makes the interpretation of the radiation pattern relatively difficult. The GG magnet on the right side of the IP is a pure dipole. The fan from this magnet can be observed in Fig. 13 in the region $x \approx -70 \ldots 0$ mm. For the misaligned beam this fan just moves up by 10 mm without changing its shape, thereby clearly indicating a vertical beam angle in GG. Unfortunately this radiation is not easily observable since it is contained in the proton beam pipe. Perhaps it will be possible to observe this fan at the location of the luminosity detector, about 90 m from the IP. A collection of transverse radiation profiles for relevant locations in the IR is given in the Appendix.

4.3 SR Emission Angle Distribution

The typical angle by which the emission direction of a photon deviates from the orbit of the emitting electron is $1/\gamma$, about $17\,\mu$rad. This angle is usually small compared to the natural angular spread of the particle beam and has been neglected in the above examples. However,
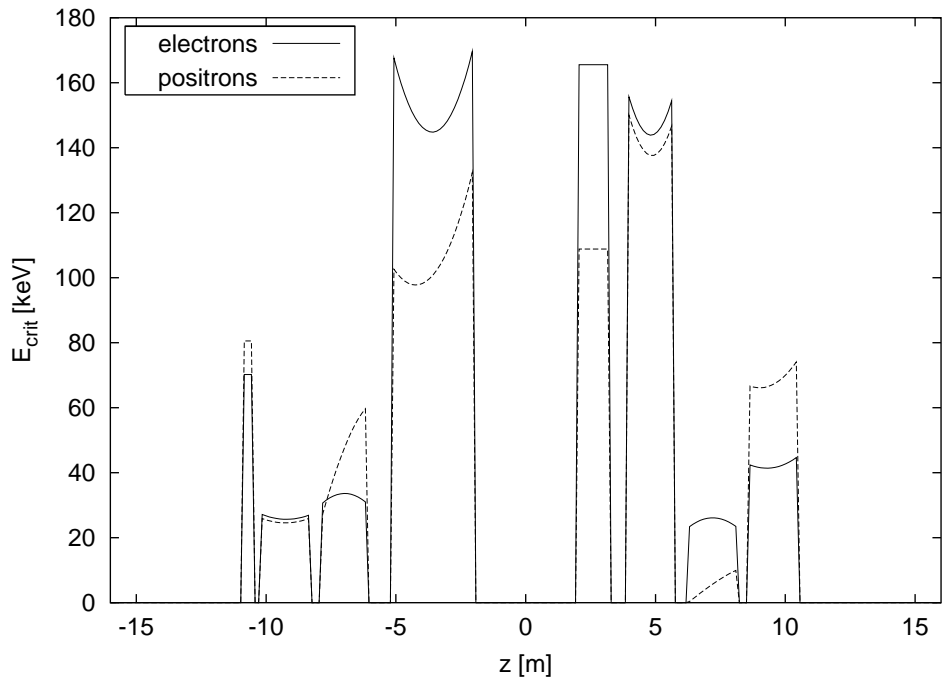
Figure 11: Critical energy of the radiation for particles on the design orbit, across the IR.
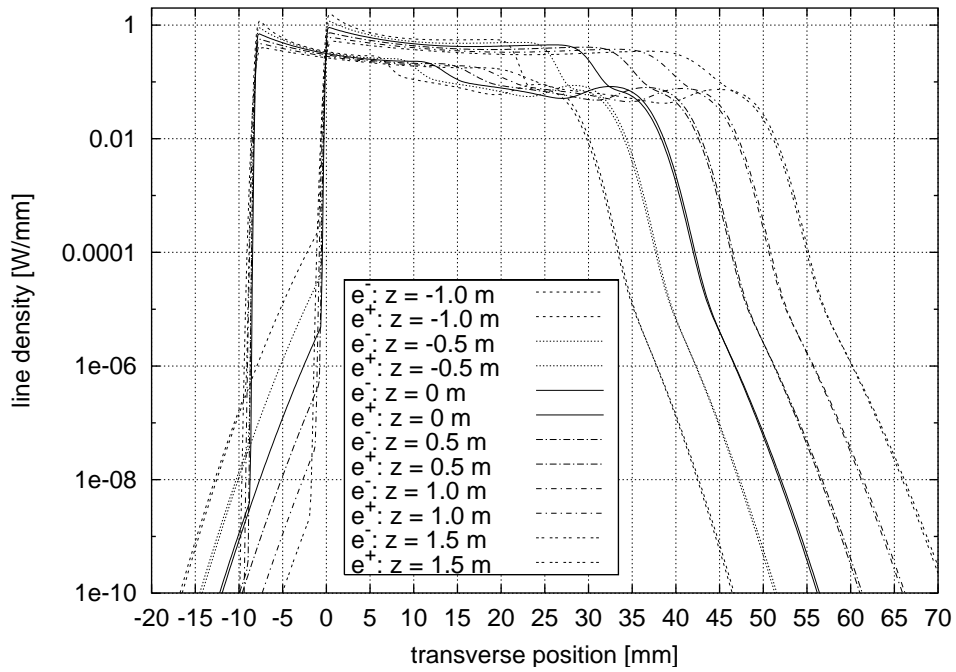
Figure 12: Several radiation profiles inside the detector for electron and positron operation.
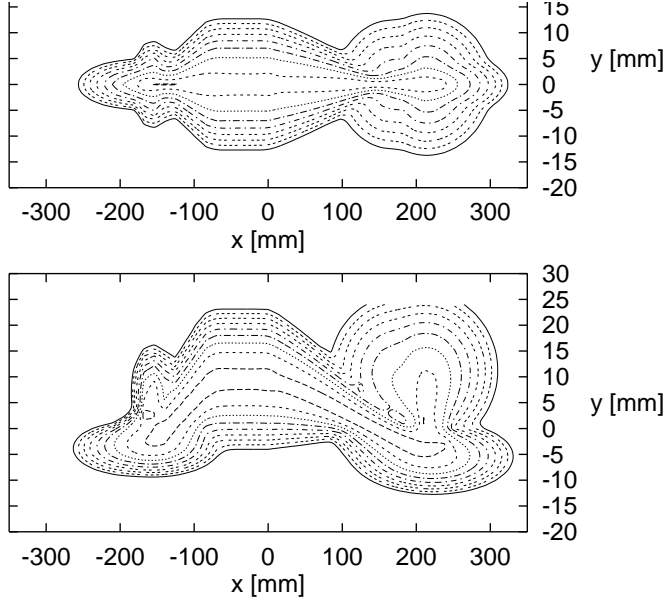
Figure 13: Two-dimensional radiation pattern as it could be seen at $24\,\mathrm{m}$ from the IP on the right side. The upper plot applies for an ideal orbit whereas the lower one assumes a vertically misaligned beam with a 3σ offset from the ideal orbit. The density scale is logarithmic and covers 8 orders of magnitude.

since we are concerned about very small probabilities we should take a closer look at the distribution. In fact the tails of the emission angle distribution fall off much slower than for instance a Gaussian distribution. According to Jackson [9] the distribution of radiated energy per unit space angle[1] and frequency of the photon is approximately given by:

$$
\frac{d^2 I}{d\omega d\Omega} \approx \frac{e^2}{3\pi^2 c}\left(\frac{\omega\rho}{c}\right)^2\left(\frac{1}{\gamma^2}+\theta^2\right)^2\left[K_{2/3}^2(\xi)+\frac{\theta^2}{1/\gamma^2+\theta^2}K_{1/3}^2(\xi)\right] \tag{3}
$$
$$
\xi = \frac{\omega\rho}{3c}\left(\frac{1}{\gamma^2}+\theta^2\right)^{\frac{3}{2}} = \frac{\omega}{\omega_c}\left(1+\gamma^2\omega^2\right)^{\frac{3}{2}}
$$

Here ω_c is the frequency that corresponds to the critical photon energy, the K's are modified Bessel functions. This expression can be analytically integrated over all frequencies, yielding the result:

$$
\frac{dI}{d\Omega} = \frac{7e^2}{16\rho}\left[\left(\frac{1}{\gamma^2}+\theta^2\right)^{-\frac{5}{2}}+\frac{5\theta^2}{7}\left(\frac{1}{\gamma^2}+\theta^2\right)^{-\frac{7}{2}}\right] \tag{4}
$$

We are interested to obtain the fractional part of energy, radiated beyond a certain angle θ_0. This can be obtained by normalizing the energy distribution with the total radiated energy $I_{\mathrm{tot}} = 4\pi e^2\gamma^4/3\rho$, and integrating over all angles from θ_0 to $\pi/2$ (note that θ is the latitude).

---

[1]In spherical coordinates θ denotes the angle between the photon and the velocity vector of the electron. The dependence on ϕ is neglected.

16

$$
\begin{aligned}
p(\theta > \theta_0) &= \frac{1}{I_{\text{tot}}} 2 \cdot 2\pi \int_{\theta_0}^{\pi/2} \cos\theta d\theta \frac{dI}{d\Omega} \approx \frac{4\pi}{I_{\text{tot}}} \int_{\theta_0}^{\infty} d\theta \frac{dI}{d\Omega} \\
&= 1 - \frac{\frac{21\theta_0}{16\gamma^4} + \frac{5\theta_0^3}{2\gamma^2} + 16\theta_0^5}{\left(\frac{1}{\gamma^2} + \theta_0^2\right)^{\frac{5}{2}}} \approx \frac{9}{16\gamma^4\theta_0^4}
\end{aligned}
\tag{5}
$$

The result for HERA energy is plotted in Fig. 14. When we look at fractional energies of 10^{-10} we find that the angle can be as large as $5\,\text{mrad}$ which is 300 (!) times $1/\gamma$. However, as was pointed out by E. Lohrmann [10], the radiation at large emission angles exhibits very long wavelengths and is thus not dangerous for the HERA experiments. We can estimate the fractional energies also with a cut in photon energy from (4). The modified Bessel functions can be approximated by exponential functions for large arguments $K_{\frac{1}{3},\frac{2}{3}}(x) \to \sqrt{\pi/2x}\exp(-x)$. Consequently, if we consider only high frequency components in the radiation, for example photon energies above one percent of the critical energy, we find the intensity to decay exponentially with larger angles.

$$
\begin{aligned}
p(\theta > \theta_0, \omega > \omega_0) &= \frac{2 \cdot 2\pi}{I_{\text{tot}}} \int_{\theta_0}^{\pi/2} \cos\theta d\theta \int_{\omega_0}^{\infty} d\omega \frac{d^2I}{d\omega d\Omega} \approx \frac{4\pi}{I_{\text{tot}}} \int_{\theta_0}^{\infty} d\theta \int_{\omega_0}^{\infty} d\omega \frac{d^2I}{d\omega d\Omega} \\
&= \frac{27\gamma}{\pi^2} \int_{\theta_0}^{\infty} d\theta \int_{\omega_0}^{\infty} \frac{d\omega}{\omega_c} \left(\frac{\omega}{\omega_c}\right)^2 (1+\gamma^2\theta^2)^2 \left[K_{2/3}^2(\xi) + \frac{\gamma^2\theta^2}{1+\gamma^2\theta^2} K_{1/3}^2(\xi)\right] \\
&\approx \frac{27\gamma}{2\pi} \int_{\theta_0}^{\infty} d\theta \frac{(1+2\gamma^2\theta^2)(1+\frac{2\omega_0}{\omega_c}(1+\gamma^2\theta^2)^{\frac{3}{2}})}{(1+\gamma^2\theta^2)^{\frac{7}{2}}} \exp\left(-\frac{2\omega_0(1+\gamma^2\theta^2)^{\frac{3}{2}}}{\omega_c}\right) \\
&\approx \frac{54\gamma}{\pi} \int_{\theta_0}^{\infty} d\theta \frac{\omega_0}{\omega_c} \frac{1}{\gamma^2\theta^2} \exp\left(-\frac{2\omega_0\gamma^3\theta^3}{\omega_c}\right) \\
&\approx \frac{54\omega_0}{\pi\omega_c} \left(\frac{2\omega_0}{\omega_c}\right)^{\frac{1}{3}} \left[1 - \Gamma\left(\frac{2}{3}, \frac{2\omega_0\gamma^3\theta_0^3}{\omega_c}\right)\right]
\end{aligned}
\tag{6}
$$

Γ in the last expression is the incomplete Gamma-function. The approximations are valid for $\theta\gamma \gg 1$ and $\xi \gg 1$, i.e. $\omega \gg \omega_c/\gamma^3\theta^3$.

5 Alignment and Orbit Correction

An important aspect of the IR layout is the ability to do efficient and accurate orbit correction on both beams, and to identify rough magnet misalignments quickly. Alignment tolerances for the upgraded IR are tighter, mainly because of the more crucial SR steering through the detectors. In order to get better control we have foreseen more detectors to obtain information on beam positions, SR fan position and magnet positions. The vertical location of the SR fan can be detected with photoelectric sensors [11] at about $25\,\text{m}$ on the right side of the IP. Furthermore we can use a screen/video-camera combination at the location of the luminosity detector, about $95\,\text{m}$ from the IP [12]. In addition there are more ways available to affect the beam orbit. Besides the standard beam steering via corrector dipoles it is also possible to move the magnet support bridges on both sides remotely, as well as the superconducting magnets inside the detectors. Of course this kind of mechanical correction cannot be done every day, because the risk of vacuum leaks or mechanical damage is too high for frequent mechanical
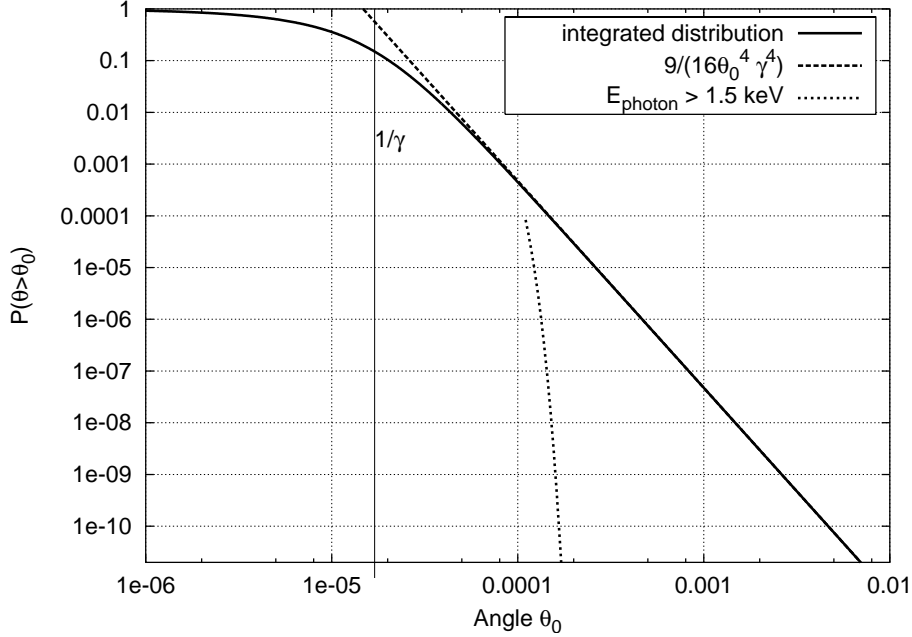
Figure 14: Fractional radiated energies for emission angles larger than θ_0, and a graph that includes a cut in the photon energy in addition.

movements. Appropriate software that integrates all the available information should give the operator a high level of confidence when he makes the decision that it is really necessary to move the magnet bridges. For example this software could provide three independent ways to determine the misalignment of the magnet bridges: First of all one can inspect the data of an online stretched wire alignment system for correlated position changes of the magnets on the bridge. Secondly one can try to correct the beam orbit as best as possible by virtually moving the magnet bridge, i.e. changing the positions of the quadrupoles on the bridge in a correlated way. If this brings a good improvement of the predicted orbit the bridge is probably misaligned. Finally it is also possible to determine the quadrupole positions with respect to the beam by so called beam based alignment techniques (BBA). If all methods give similar answers for the magnet bridge misalignments one can correct the position of the bridge remotely.

Beam position monitors (BPM's) have to be provided in sufficient number and distribution to allow representative sampling of the orbit, and of course also a sufficient arrangement of corrector dipoles is needed. To test monitor and corrector arrangement, orbit correction scenarios have been simulated numerically. The quadrupoles in the beamline are misaligned by random amounts, then the orbit through the misaligned magnets is computed. Next the orbit is corrected as best as possible, using the given information from the BPM's and the available correctors. Finally the quality of the corrected orbit is assessed by computing an rms deviation value. The whole procedure is repeated for different seeds of misaligned magnet arrangements. In this context another point of interest is the question whether the real orbit is sampled sufficiently enough with the assumed BPM arrangement. This can be assessed by computing the rms orbit once from the BPM values and once from all meshpoints the code knows (a lot more). In case of representative sampling both values should agree well. Fig. 16 shows the results of such simulations for the lepton beam. The magnets are randomly misaligned according to a Gaussian distribution with an rms value of $150\,\mu$m. The distribution is cut-off at $300\,\mu$m. The
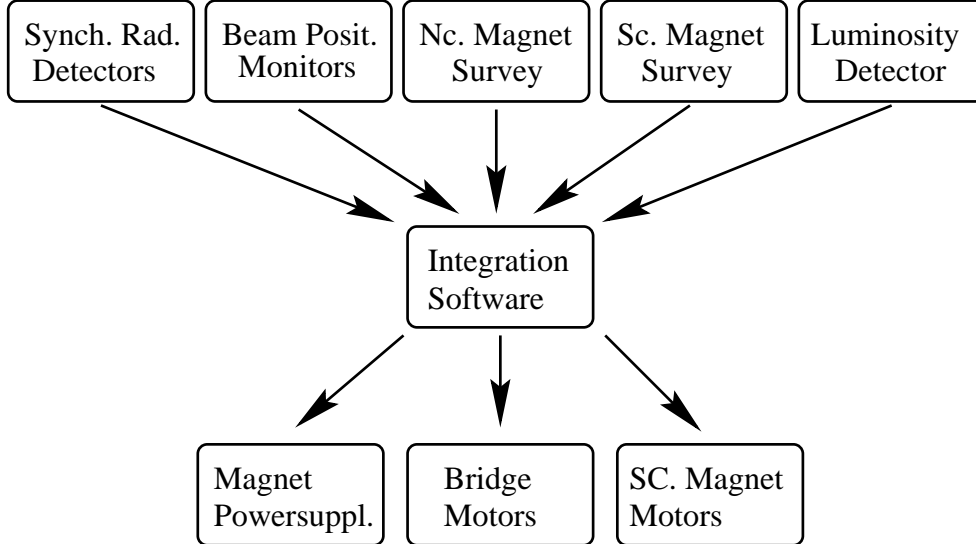
Figure 15: Data flow in the IR orbit steering scheme.

BPM's have been misaligned by the same rms amount, i.e. their measurements are assumed to be wrong by adding random numbers. On the plots we find that the rms values from the BPM readings agree pretty well with the rms values from all meshpoints, which indicates good sampling. Furthermore the rms values of the corrected orbits are of the order of $100 \ldots 200 \, \mu\mathrm{m}$ which is sufficiently good. The values before correction are so large that it is probably impossible to store a beam in a first attempt, i.e. first turn steering has to be done step by step around the machine. However, this is not unusual also for the present lattice. Table 4 gives an overview on the BPM's and correctors in the IR.

More detailed simulations, also for the proton beam, have been performed by Ch. Montag [13]. The effects of misalignments on the beam polarization were investigated by E. Gianfelice [14] and M. Berglund [5]. Fig. 15 shows a schematic overview on all sources of information and all actuators that can be used to act back on the beam. The mathematical scheme to include mixed information on orbit position (BPM's) and orbit angles (SR-detectors) in the correction algorithm is described in the next section.

5.1 Orbit Correction Algorithms

5.1.1 Using Dipoles and BPM's only

We repeat here the basic algorithm that is applied to simulate orbit correction and that is commonly used also in practice. The measured beam position at a particular location with index k is given by a sum of two contributions - the orbit distortion resulting from quadrupole misalignments in the machine, and a part initiated by the corrector dipole settings. The goal is to choose the corrector settings such that the BPM readings are zeroed.

$$x_k^{\mathrm{BPM}} = x_k^{\mathrm{mis}} + x_k^{\mathrm{corr}} \overset{!}{=} 0 \tag{7}$$

The corrector contribution is given by:

$$x_k^{\mathrm{corr}} = \sum_i \theta_i \frac{\sqrt{\beta_i \beta_k}}{2 \sin(\pi Q)} \cos(|\phi_i - \phi_k| - \pi Q) \tag{8}$$

19
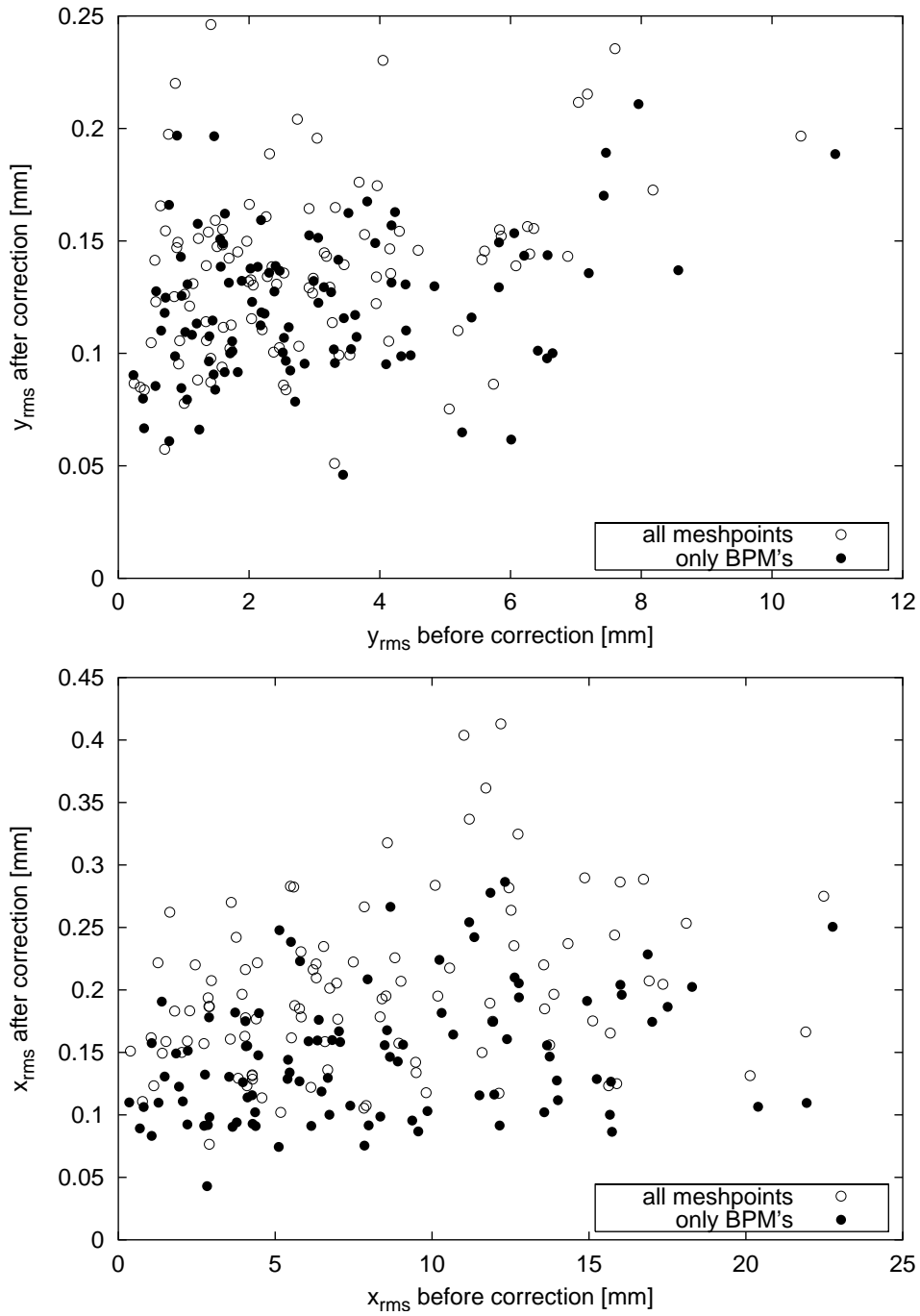
Figure 16: Results of an electron orbit correction simulation, vertical plane (upper) and horizontal plane. Rms beam-orbit deviations before and after applying correction. Each dot represents another random seed of misaligned quadrupoles. Details see text.

BPM Position [m]	Protons			Electrons		
	x	x_{off} [mm]	y	x	x_{off} [mm]	y
-10.957				×	3.0	×
-5.898	×	18.4	×	×	0.0	×
-1.705 N	×	0.0	×	×	0.0	×
-1.614 S	×	3.0	×	×	3.0	×
+1.655 N	(×)	20/28	×	(×)	20/28	×
+1.612 S	(×)	17.4	×	(×)	17.4	×
+14.600				×	3.0	×
±26.932				×	0.0	×
±43.605				×	0.0	×
±54.302				×	0.0	×
±27.000	×	2.4	×			
±41.000	×	0.0	×			
±61.000	×	0.0	×			

Corrector Position [m]		Protons		Electrons	
		x	y	x	y
BO*	-10.680			×	
GO	-3.600			×	×
GG	+2.600			×	×
CV	±27.199				×
CH	±43.917			×	
CV	±55.747				×
CV	±61.984				×
BH*	±64.212			×	
BQ*	±18.880	×			
BW*	±26.590	×			
BZ	±27.680		×		
BZ	±55.648		×		
BP*	±56.596	×			

Table 4: BPM and corrector positions across the IR. Negative position numbers are located on the left side of the IP. The monitors marked with brackets might have problems to measure the horizontal position since the nominal beam position is far off-center in the vacuum chamber. Some of the monitors are mounted not symmetrically with respect to the beam, i.e. their measurements exhibit a systematic offset. The offset of the nominal beam position with respect to the electrical center of the monitor is given in the table. The magnets marked with a star (*) have nonzero default values, i.e. are not exclusively used as corrector dipoles.

Here θ_i is the kick angle of the i'th corrector and Q the tune of the machine. The index k enumerates the observer, i.e. BPM locations. Consequently we have to solve the following vector equation to do orbit correction:

$$
\begin{aligned}
\vec{x}_{\mathrm{BPM}} &= \vec{x}_{\mathrm{mis}} + \mathbf{M}\vec{\theta} = \mathbf{0} \\
\vec{\theta} &= -\mathbf{M}^{-1}\vec{x}_{\mathrm{mis}}
\end{aligned}
\tag{9}
$$

For a quadratic matrix $\mathbf{M}$ this equation can be solved straight forward, however, often the number of monitors and correctors is not exactly equal, or the matrix is degenerate, i.e. not invertible. In such a situation one can use a singular value decomposition (SVD) of $\mathbf{M}$ for the matrix "inversion" [15]:

$$
\begin{aligned}
\mathbf{M} &= \mathbf{U}\lambda\mathbf{V^T} \\
\mathbf{M^{-1}} &= \mathbf{V}\lambda^{-1}\mathbf{U^T}
\end{aligned}
\tag{10}
$$

The SVD yields two orthogonal matrices, $\mathbf{U}$ and $\mathbf{V}$, and a diagonal matrix λ. In case the matrix is degenerate, some elements in λ will be zero. For the inversion the reciprocals of those elements have to be set to zero also. This way to invert the matrix leads to a satisfactory result for all three possible cases: 1.) There are more monitors than correctors, the problem is over-determined, in general there is no corrector setting to zero all BPM's at the same time. In this case the SVD provides the solution with minimal rms-deviation. 2.) There are exactly as

Motor	z-location
left bridge, left side, horizontal	-10.895
left bridge, left side, vertical	-10.745
ZEUS, left bridge, right side, horizontal	-7.170
ZEUS, left bridge, right side, vertical	-7.170
H1, left bridge, right side, horizontal	-6.909
H1, left bridge, right side, vertical	-6.909
right bridge, left side, horizontal	5.480
right bridge, left side, vertical	5.025
right bridge, right side, horizontal	10.055
right bridge, right side, vertical	9.655

Table 5: Longitudinal positions of the motors that can move the magnet bridges.

many monitors as correctors and no degeneracies in the matrix - the SVD provides the exact solution. 3.) More correctors than needed - the SVD solves the problem exactly and minimizes the length of the vector $\vec{\theta}$ at the same time, i.e. the smallest corrector strengths are used.

Of course in practice the problem can be slightly more difficult, for instance if kick strength limits have to be taken into account. Also for this problem the SVD might give a useful hint. When the problem is under-determined there exists a certain degree of freedom to vary the solution vector without violating equation (9). A linear combination of all column vectors in matrix $\mathbf{V}$, for which the corresponding elements in λ are zero, can be added to the solution vector $\vec{\theta}$ without changing the validity of the solution. One can try now to use this flexibility in such a way as to satisfy the boundary conditions given by the maximum currents of the corrector power supplies [16].

5.1.2 Using SR Detectors and Bridge Motors in Addition

This is a generalization of the above section and should be considered as an upgrade of the standard scheme. Measurement of the vertical position of the SR fan gives information on the orbit angle at the position where the fan is radiated. This information can also be fed into the orbit correction scheme. The beam angle deviation at location k as a function of the corrector settings is given by:

$$
\begin{aligned}
x_k'^{\,\mathrm{corr}} &= -\sum_i \frac{\theta_i}{2\sin(\pi Q)} \sqrt{\frac{\beta_i}{\beta_k}} \left[\alpha_k \cos(|\phi_i - \phi_k| - \pi Q) + \mathrm{sign}(\phi_k - \phi_i) \sin(|\phi_i - \phi_k| - \pi Q) \right] \\
&= -\sum_i \frac{\theta_i \sqrt{\beta_i \gamma_k}}{2\sin(\pi Q)} \cos \left[|\phi_i - \phi_k| - \pi Q - \mathrm{sign}(\phi_k - \phi_i) \arctan(1/\alpha_k) \right]
\end{aligned} \tag{11}
$$

These equations together with (8) can be used to make up a matrix that corrects BPM measurements and SR-angle measurements at the same time. For over-determined systems, where the SVD computes a solution with minimal rms deviation, above equation should be scaled with $\sqrt{\beta_k/\gamma_k}$ in order to obtain something like an equivalent beam offset from the angle. Otherwise BPM readings and beam angles would have an inadequate weighting for the optimum solution.

The magnet bridges on both sides of the detectors are equipped with motors that allow to vary the bridge position, both vertically and horizontally. Obviously one would not try to

move the bridge for every orbit correction. The locations of the individual bridge motors are given in table 5. A special case is the right end of the left bridge were the bridge rests on a A-shaped stand. The two legs of this stand are equipped with vertically pushing motors that allow vertical bridge movements through parallel motions, or horizontal movements through differential motions. The location of the A-stand differs for ZEUS and H1.

Adjustments of the bridge motors lead to a correlated position change of two quadrupoles on the left side of the IP and three on the right side. The question is here what transverse motor positions at entrance, x_a, and exit, x_e, of the bridges should be chosen to correct the orbit best. Transverse means horizontally or vertically. The position of the l'th quadrupole on the bridge is computed from the motor positions as follows:

$$x_l = x_a \frac{z_e - z_l}{z_e - z_a} + x_e \frac{z_l - z_a}{z_e - z_a} \tag{12}$$

Here z_a, z_e, z_l are the longitudinal positions of the bridge motors and the effective center of the considered quadrupole, K_l is the quad strength. The effect on the beam at index k is then given by:

$$
\begin{aligned}
x_k^{\mathrm{corr}} &= \sum_l K_l \frac{\sqrt{\beta_l \beta_k}}{2 \sin(\pi Q)} \left(x_a \frac{z_e - z_l}{z_e - z_a} + x_e \frac{z_l - z_a}{z_e - z_a} \right) \cos(|\phi_l - \phi_k| - \pi Q) \\
&= c_a x_a + c_e x_e
\end{aligned}
\tag{13}
$$

This is an additional linear equation that can be added to (8) to minimize the BPM readings. A similar problem as for including the SR-angles into the set of equations arises here from the fact that corrector angles and motor offsets with completely different units and magnitudes are components of the solution vector and are treated in the same way. For the under-determined system the SVD minimizes the length of the solution vector, and this would lead to wrong weighting of motor set-values and corrector angles. A possible solution would be to scale the motor values to equivalent angles using typical magnet K-values. Effects of bridge misalignments/deformations and their correction are investigated in detail within the framework of a diploma thesis by F. Stulle [17].

6   Appendix

6.1   Brief Description of Geometry Code

The code, which is written in C++, was specifically developed to compute the HERA interaction region geometry. For common programs like MAD this would be a nonstandard task since the positions of the common magnets have to be determined relatively to the electron beam, whereas the proton beam passes them with odd angles and offsets. Furthermore the program should be capable to do some other nonstandard computations as listed below.
Capabilities of the HERA IR geometry code:

- computation of the beam orbit in combined function magnets with the magnet coordinates given either relative to the beam orbit or absolute in space

- very general parameter fitting capabilities; unlimited number of varied parameters and fit conditions; side conditions possible; functions of parameters possible

- computation of one- and two dimensional projected synchrotron radiation patterns (power densities)

- simulation and test of orbit correction algorithms

The program reads magnet arrangement and beam parameters from MAD like input files and produces (if desired) a set of output files for example with magnet-, optics- and geometry tables or graphs. The program consists of the following modules: optic.cc (optics and geometry + fitting routines), io.cc (input/output routines), synch.cc (SR code), orbcorr.cc (orbit correction), main.cc (user adjustable main program).

The computation of the interaction region is done in the following order:

1. calculation of the positron orbit, starting from the IP ($x = -7.5$ mm) for the left and right sides separately; magnet positions given relative to the beam; left side is then inverted and the right side attached to it; the now determined absolute magnet positions are stored in a file

2. proton orbit for positron operation; use absolute positions for common magnets (read from file) and relative positions for exclusive proton magnets

3. electron beam - use absolute positions for the common magnets with some offsets added to the quadrupoles in order to match the orbit to the positron case

4. proton orbit for electron operation

5. proton orbit for injection energy (40 GeV); use absolute magnet positions determined by the high energy cases

A detailed description of the code and the syntax of input files would be too long and inadequate for this report. A separate internal note will describe the code in such a way as to allow "non-experts" to recompute the IR.

6.2   Beam Orbit

In the following sections we print the orbits for the four involved beams, i.e. electrons, positrons and the corresponding proton beams. Each table shows two beams, the lepton and the proton beam. The first two columns contain the names of the beamline elements for the protons and the leptons, the corresponding z-position is displayed in column 3. An element name is only displayed if the beamline has an element at the particular z-position. The next columns contain $x, x', 12\sigma_x, y, y', 12\sigma_y$ for the proton beam. The coordinate system is explained in Fig. 17. The last four columns contain $x, x', 20\sigma_x, 20\sigma_y$ for the lepton beam (the lepton beams experience no vertical deflection).

6.2.1   Electrons and Protons

p-beam	e-beam	Z	Xp	Xp'	12sx	Yp	Yp'	12sy	Xe	Xe'	20sx	20sy
		[m]	[mm]	[mrad]	[mm]	[mm]	[mrad]	[mm]	[mm]	[mrad]	[mm]	[mm]
START		-89.045	15.8	0.00	19.1	96.7	-5.74	2.0				
DL30p		-79.045	15.8	0.00	24.7	39.3	-5.74	3.9				
BUL77		-74.945	15.8	0.00	27.0	19.7	-3.83	5.9				
DL29p		-74.255	15.8	0.00	27.4	17.0	-3.83	6.3				
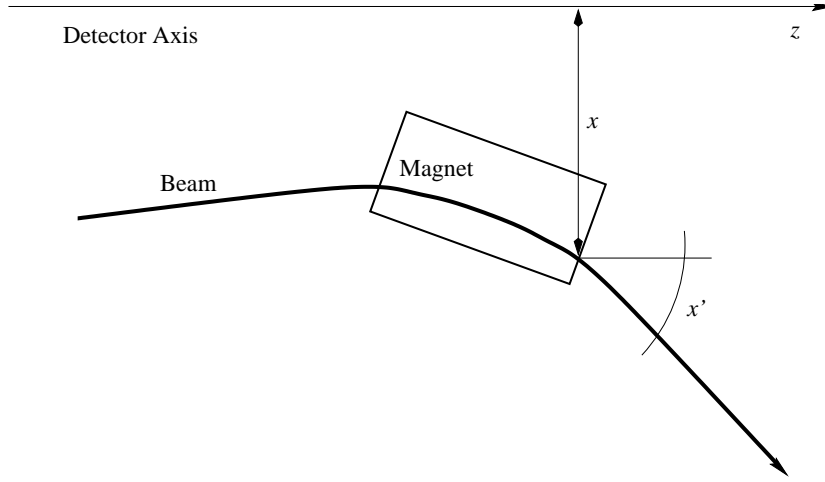
Figure 17: The beam coordinates are given at the end of each element, going from the left side of the IP to the right. The z-axis is a tangent to the beams in the IP.

```
BUL72          -70.155   15.8   0.00 29.7    5.2  -1.91  8.3
DL28p          -69.465   15.8   0.00 30.1    3.9  -1.91  8.7
        START -68.598   15.8   0.00 30.6    2.4  -1.51  9.1 -525.5  10.00 11.4  3.2
          DL20 -67.598   15.8   0.00 31.2    1.2  -1.04  9.6 -515.5  10.00 11.1  3.8
         QLL67 -66.598   15.8   0.00 31.7    0.4  -0.58 10.1 -505.5  10.00 12.0  4.1
          DL19 -65.889   15.8   0.00 32.1    0.1  -0.25 10.5 -498.4  10.00 13.3  4.1
BUL67          -65.365   15.8   0.00 32.4    0.0   0.00 10.8 -493.3   9.54 14.3  4.1
DL27p          -64.513   15.8   0.00 32.9    0.0   0.00 11.2 -485.5   8.81 16.0  4.1
         BHL64 -62.531   15.8   0.00 33.5    0.0   0.00 12.4 -469.7   7.09 19.9  4.2
          DL18 -62.132   15.8   0.00 33.5    0.0   0.00 12.6 -466.9   7.09 20.7  4.3
         CVL62 -61.832   15.8   0.00 33.5    0.0   0.00 12.9 -464.8   7.09 21.3  4.3
          DL17 -61.665   15.8   0.00 33.5    0.0   0.00 13.0 -463.6   7.09 21.6  4.3
QRL63          -61.513   15.8   0.00 33.5    0.0   0.00 13.1 -462.5   7.09 21.9  4.4
DL26p          -61.065   15.8   0.00 33.4    0.0   0.00 13.4 -459.3   7.09 22.1  4.6
 MPL4          -61.065   15.8   0.00 33.4    0.0   0.00 13.4 -459.3   7.09 22.1  4.6
         QLL61 -60.665   15.8   0.00 33.3    0.0   0.00 13.8 -456.5   7.09 21.6  4.9
DL25p          -60.552   15.8   0.00 33.3    0.0   0.00 13.8 -455.7   7.09 21.4  5.0
QRL59          -57.552   15.8   0.00 31.6    0.0   0.00 16.7 -434.4   7.09 15.4  8.0
DL24p          -57.096   15.8   0.00 31.2    0.0   0.00 17.2 -431.2   7.09 14.6  8.5
BPL57          -56.096   15.6  -0.40 30.3    0.0   0.00 18.3 -424.1   7.09 12.6  9.5
          DL16 -55.895   15.5  -0.40 30.1    0.0   0.00 18.5 -422.7   7.09 12.3  9.7
DL23p          -55.798   15.5  -0.40 30.0    0.0   0.00 18.6 -422.0   7.09 12.1  9.8
         CVL56 -55.595   15.4  -0.40 29.8    0.0   0.00 18.9 -420.5   7.09 11.7 10.0
BZL56          -55.498   15.4  -0.40 29.8    0.0   0.00 19.0 -419.8   7.09 11.5 10.1
          DL15 -55.428   15.3  -0.40 29.7    0.0   0.00 19.0 -419.4   7.09 11.4 10.2
         QLL55 -54.428   14.9  -0.40 28.8    0.0   0.00 20.2 -412.3   7.09 10.2 10.5
DL22p          -54.335   14.9  -0.40 28.7    0.0   0.00 20.3 -411.6   7.09 10.2 10.5
          DL14 -54.198   14.8  -0.40 28.6    0.0   0.00 20.4 -410.6   7.09 10.1 10.5
          MEL4 -54.198   14.8  -0.40 28.6    0.0   0.00 20.4 -410.6   7.09 10.1 10.5
QRL53          -51.335   13.7  -0.40 26.9    0.0   0.00 22.9 -390.3   7.09  9.2  9.6
DL21p          -50.985   13.6  -0.40 26.7    0.0   0.00 23.2 -387.8   7.09  9.1  9.5
QRL49          -47.985   12.4  -0.40 26.7    0.0   0.00 24.3 -366.6   7.09  9.2  8.6
DL20p          -47.550   12.2  -0.40 26.8    0.0   0.00 24.4 -363.5   7.09  9.2  8.5
          DL13 -43.966   10.7  -0.40 29.3    0.0   0.00 23.5 -338.1   7.09 10.5  7.4
```

p-beam	e-beam	Z [m]	Xp [mm]	Xp' [mrad]	12sx [mm]	Yp [mm]	Yp' [mrad]	12sy [mm]	Xe [mm]	Xe' [mrad]	20sx [mm]	20sy [mm]
GBL46		-43.700	10.6	-0.40	29.6	0.0	0.00	23.3	-336.2	7.09	10.7	7.4
	CHL44	-43.666	10.6	-0.40	29.6	0.0	0.00	23.3	-336.0	7.09	10.7	7.4
	DL12	-43.604	10.6	-0.40	29.7	0.0	0.00	23.2	-335.5	7.09	10.7	7.3
	MEL3	-43.604	10.6	-0.40	29.7	0.0	0.00	23.2	-335.5	7.09	10.7	7.3
	DL11	-43.499	10.6	-0.40	29.8	0.0	0.00	23.2	-334.8	7.09	10.8	7.3
	QLL43	-42.499	10.2	-0.40	31.0	0.0	0.00	22.5	-327.7	7.09	11.1	7.2
	DL10	-42.239	10.1	-0.40	31.3	0.0	0.00	22.3	-325.8	7.09	11.1	7.2
DL19p		-41.000	9.6	-0.40	32.7	0.0	0.00	21.5	-316.3	8.34	11.2	7.4
MPL3		-41.000	9.6	-0.40	32.7	0.0	0.00	21.5	-316.3	8.34	11.2	7.4
	BNL41	-40.739	9.5	-0.40	33.1	0.0	0.00	21.3	-314.1	8.60	11.3	7.4
DL18p		-40.440	9.3	-0.40	33.4	0.0	0.00	21.1	-311.5	8.60	11.3	7.4
GBL39		-36.590	7.8	-0.40	35.8	0.0	0.00	19.9	-278.4	8.60	12.4	7.8
DL17p		-36.240	7.7	-0.40	35.9	0.0	0.00	19.8	-275.4	8.60	12.5	7.9
GBL34		-32.390	6.1	-0.40	33.9	0.0	0.00	21.0	-242.3	8.60	14.3	8.4
DL16p		-32.040	6.0	-0.40	33.6	0.0	0.00	21.2	-239.3	8.60	14.4	8.4
p-beam	e-beam	Z [m]	Xp [mm]	Xp' [mrad]	12sx [mm]	Yp [mm]	Yp' [mrad]	12sy [mm]	Xe [mm]	Xe' [mrad]	20sx [mm]	20sy [mm]
GAL30		-28.190	4.4	-0.40	27.5	0.0	0.00	25.0	-206.1	8.60	16.6	9.0
DL15p		-27.830	4.3	-0.40	26.8	0.0	0.00	25.5	-203.0	8.60	16.8	9.0
BZL28		-27.530	4.2	-0.40	26.2	0.0	0.00	25.9	-200.5	8.60	17.0	9.1
	DL9	-27.348	4.1	-0.40	25.8	0.0	0.00	26.2	-198.9	8.60	17.1	9.1
	CVL27	-27.048	4.0	-0.40	25.2	0.0	0.00	26.6	-196.3	8.60	17.3	9.1
DL14p		-27.000	4.0	-0.40	25.1	0.0	0.00	26.6	-195.9	8.60	17.3	9.2
MPL2		-27.000	4.0	-0.40	25.1	0.0	0.00	26.6	-195.9	8.60	17.3	9.2
DL13p		-26.890	3.9	-0.40	24.9	0.0	0.00	26.8	-195.0	8.60	17.4	9.2
	DL8	-26.889	3.9	-0.40	24.9	0.0	0.00	26.8	-195.0	8.60	17.4	9.2
	MEL2	-26.889	3.9	-0.40	24.9	0.0	0.00	26.8	-195.0	8.60	17.4	9.2
BWL27		-26.290	3.7	-0.48	23.7	0.0	0.00	27.6	-189.8	8.60	17.7	9.3
DL12p		-25.730	3.4	-0.48	22.5	0.0	0.00	28.3	-185.0	8.60	18.1	9.4
GNL25		-23.800	2.4	-0.55	19.0	0.0	0.00	30.4	-168.4	8.60	19.3	9.7
DL11p		-23.550	2.3	-0.55	18.6	0.0	0.00	30.6	-166.2	8.60	19.5	9.7
GNL23		-21.620	1.1	-0.65	15.7	0.0	0.00	31.6	-149.6	8.60	20.8	10.0
DL10p		-21.370	0.9	-0.65	15.4	0.0	0.00	31.7	-147.5	8.60	21.0	10.1
GNL20		-19.440	-0.4	-0.76	13.1	0.0	0.00	31.5	-130.9	8.60	22.3	10.4
DL9p		-19.200	-0.6	-0.76	12.8	0.0	0.00	31.4	-128.8	8.60	22.4	10.5
BQL19		-18.560	-1.0	-0.57	12.1	0.0	0.00	31.2	-123.3	8.60	22.9	10.6
DL8p		-18.220	-1.2	-0.57	11.8	0.0	0.00	31.0	-120.4	8.60	23.1	10.6
GML17		-14.820	-2.5	-0.15	8.7	0.0	0.00	28.2	-91.2	8.60	25.5	11.3
DL7p		-14.580	-2.5	-0.15	8.5	0.0	0.00	27.9	-89.1	8.60	25.7	11.3
GML13		-11.180	-2.3	0.25	6.3	0.0	0.00	22.4	-59.8	8.60	28.2	12.0
	DL7	-11.180	-2.3	0.25	6.3	0.0	0.00	22.4	-59.8	8.60	28.2	12.0
ALGM		-10.954	-2.3	0.25	6.2	0.0	0.00	22.0	-57.9	8.60	28.3	12.0
DLM		-10.931	-2.3	0.25	6.2	0.0	0.00	21.9	-57.7	8.60	28.4	12.0
	ALGM	-10.930	-2.3	0.25	6.2	0.0	0.00	21.9	-57.7	8.60	28.4	12.0
BOL11	BOL11	-10.431	-2.1	0.24	5.9	0.0	0.00	20.9	-53.6	8.01	28.7	12.1
DL6	DL6	-10.182	-2.1	0.24	5.8	0.0	0.00	20.4	-51.6	8.01	28.9	12.2
GJL9	GJL9	-8.302	-1.3	0.53	4.8	0.0	0.00	16.6	-37.3	7.19	37.4	9.8
DL5	DL5	-7.930	-1.1	0.53	4.6	0.0	0.00	15.8	-34.6	7.19	40.7	8.8
GIL7	GIL7	-6.050	-0.5	0.19	3.6	0.0	0.00	12.0	-20.1	8.21	38.3	7.2
DL4	DL4	-5.740	-0.4	0.19	3.5	0.0	0.00	11.4	-17.6	8.21	34.8	7.5
MPL1	MEL1	-5.740	-0.4	0.19	3.5	0.0	0.00	11.4	-17.6	8.21	34.8	7.5
DL3	DL3	-5.200	-0.3	0.19	3.2	0.0	0.00	10.4	-13.1	8.21	28.9	7.9
GOL4	GOL4	-2.000	0.0	0.00	1.7	0.0	0.00	4.1	0.0	0.00	7.8	5.0
DL2	DL2	-1.600	0.0	0.00	1.6	0.0	0.00	3.3	0.0	0.00	6.4	4.0

p-beam	e-beam	Z [m]	Xp [mm]	Xp' [mrad]	12sx [mm]	Yp [mm]	Yp' [mrad]	12sy [mm]	Xe [mm]	Xe' [mrad]	20sx [mm]	20sy [mm]
MPL0	MEL0	-1.600	0.0	0.00	1.6	0.0	0.00	3.3	0.0	0.00	6.4	4.0
DL1	DL1	0.000	0.0	0.00	1.3	0.0	0.00	0.4	0.0	0.00	2.4	0.6
IP	IP	0.000	0.0	0.00	1.3	0.0	0.00	0.4	0.0	0.00	2.4	0.6
DR1	DR1	1.600	0.0	0.00	1.6	0.0	0.00	3.3	0.0	0.00	6.4	4.0
MPR0	MER0	1.600	0.0	0.00	1.6	0.0	0.00	3.3	0.0	0.00	6.4	4.0
DR2	DR2	1.950	0.0	0.00	1.7	0.0	0.00	4.0	0.0	0.00	7.6	4.8
GGR3	GGR3	3.250	-0.1	-0.11	2.2	0.0	0.00	6.6	-2.3	-3.59	12.4	8.0
DR3	DR3	3.500	-0.1	-0.11	2.3	0.0	0.00	7.1	-3.2	-3.59	13.3	8.6
DR4	DR4	3.852	-0.1	-0.11	2.5	0.0	0.00	7.8	-4.5	-3.59	14.6	9.5
GIR5	GIR5	5.732	-0.4	-0.13	3.4	0.0	0.00	11.5	-15.7	-8.26	28.7	10.0
DR5	DR5	6.253	-0.4	-0.13	3.7	0.0	0.00	12.5	-20.0	-8.26	35.1	8.9
GIR7	GIR7	8.133	-1.0	-0.50	4.7	0.0	0.00	16.2	-34.7	-7.47	39.9	9.1
DR6	DR6	8.567	-1.2	-0.50	4.9	0.0	0.00	17.1	-38.0	-7.47	36.5	10.0
GJR10	GJR10	10.447	-2.0	-0.25	5.9	0.0	0.00	21.0	-53.3	-8.80	29.0	11.8
AABS	AABS	10.692	-2.0	-0.25	6.0	0.0	0.00	21.5	-55.4	-8.80	28.8	11.7
EABS	EABS	10.977	-2.1	-0.25	6.2	0.0	0.00	22.0	-57.9	-8.80	28.7	11.6
p-beam	e-beam	Z [m]	Xp [mm]	Xp' [mrad]	12sx [mm]	Yp [mm]	Yp' [mrad]	12sy [mm]	Xe [mm]	Xe' [mrad]	20sx [mm]	20sy [mm]
DRM	DRM	11.000	-2.1	-0.25	6.2	0.0	0.00	22.1	-58.1	-8.80	28.7	11.5
	MER1	11.000	-2.1	-0.25	6.2	0.0	0.00	22.1	-58.1	-8.80	28.7	11.5
ARGM	ARGM	11.180	-2.1	-0.25	6.3	0.0	0.00	22.4	-59.7	-8.80	28.5	11.5
GMR13		14.580	-2.3	0.16	8.5	0.0	0.00	28.0	-89.7	-8.80	26.5	10.2
DR7p		14.820	-2.2	0.16	8.7	0.0	0.00	28.3	-91.8	-8.80	26.4	10.1
GMR17		18.220	-1.0	0.59	11.8	0.0	0.00	31.1	-121.7	-8.80	24.4	8.9
DR8p		18.560	-0.8	0.59	12.1	0.0	0.00	31.2	-124.7	-8.80	24.2	8.8
BQR19		19.200	-0.3	0.72	12.8	0.0	0.00	31.4	-130.3	-8.80	23.8	8.6
DR9p		19.440	-0.2	0.72	13.0	0.0	0.00	31.5	-132.4	-8.80	23.7	8.5
GNR20		21.370	1.1	0.61	15.3	0.0	0.00	31.7	-149.4	-8.80	22.6	7.8
DR10p		21.620	1.3	0.61	15.7	0.0	0.00	31.7	-151.6	-8.80	22.4	7.7
GNR23		23.550	2.4	0.52	18.5	0.0	0.00	30.7	-168.6	-8.80	21.4	7.1
DR11p		23.800	2.5	0.52	18.9	0.0	0.00	30.5	-170.8	-8.80	21.3	7.0
GNR25		25.730	3.4	0.44	22.5	0.0	0.00	28.4	-187.8	-8.80	20.2	6.4
DR12p		26.290	3.7	0.44	23.6	0.0	0.00	27.6	-192.7	-8.80	19.9	6.2
	DR7	26.889	3.9	0.40	24.8	0.0	0.00	26.8	-198.0	-8.80	19.6	6.1
	MER2	26.889	3.9	0.40	24.8	0.0	0.00	26.8	-198.0	-8.80	19.6	6.1
BWR27		26.890	3.9	0.40	24.8	0.0	0.00	26.8	-198.0	-8.80	19.6	6.1
DR13p		27.000	4.0	0.40	25.1	0.0	0.00	26.7	-198.9	-8.80	19.6	6.0
MPR2		27.000	4.0	0.40	25.1	0.0	0.00	26.7	-198.9	-8.80	19.6	6.0
	DR8	27.048	4.0	0.40	25.2	0.0	0.00	26.6	-199.4	-8.80	19.5	6.0
	CVR27	27.348	4.1	0.40	25.8	0.0	0.00	26.2	-202.0	-8.80	19.4	5.9
DR14p		27.530	4.2	0.40	26.1	0.0	0.00	25.9	-203.6	-8.80	19.3	5.9
BZR28		27.830	4.3	0.40	26.7	0.0	0.00	25.5	-206.2	-8.80	19.1	5.8
DR15p		28.190	4.4	0.40	27.5	0.0	0.00	25.1	-209.4	-8.80	19.0	5.7
GAR30		32.040	6.0	0.40	33.5	0.0	0.00	21.3	-243.3	-8.80	17.1	4.7
DR16p		32.390	6.1	0.40	33.9	0.0	0.00	21.0	-246.4	-8.80	17.0	4.6
GBR34		36.240	7.7	0.40	35.8	0.0	0.00	19.9	-280.3	-8.80	15.4	4.1
DR17p		36.590	7.8	0.40	35.8	0.0	0.00	19.9	-283.3	-8.80	15.3	4.1
GBR39		40.440	9.3	0.40	33.3	0.0	0.00	21.2	-317.2	-8.80	14.1	4.1
	DR9	40.739	9.5	0.40	33.0	0.0	0.00	21.4	-319.9	-8.80	14.0	4.1
DR18p		41.000	9.6	0.40	32.7	0.0	0.00	21.6	-322.1	-8.46	13.9	4.1
MPR3		41.000	9.6	0.40	32.7	0.0	0.00	21.6	-322.1	-8.46	13.9	4.1
	BNR41	42.239	10.1	0.40	31.2	0.0	0.00	22.4	-331.6	-6.83	13.6	4.3
	DR10	42.499	10.2	0.40	30.9	0.0	0.00	22.6	-333.4	-6.83	13.6	4.3
	QLR43	43.499	10.6	0.40	29.7	0.0	0.00	23.2	-340.2	-6.83	13.2	4.6

p-beam	e-beam	Z	Xp	Xp'	12sx	Yp	Yp'	12sy	Xe	Xe'	20sx	20sy
		[m]	[mm]	[mrad]	[mm]	[mm]	[mrad]	[mm]	[mm]	[mrad]	[mm]	[mm]
	DR11	43.604	10.6	0.40	29.6	0.0	0.00	23.3	-340.9	-6.83	13.1	4.6
	MER3	43.604	10.6	0.40	29.6	0.0	0.00	23.3	-340.9	-6.83	13.1	4.6
	DR12	43.666	10.6	0.40	29.5	0.0	0.00	23.3	-341.3	-6.83	13.1	4.6
DR19p		43.700	10.6	0.40	29.5	0.0	0.00	23.4	-341.5	-6.83	13.1	4.6
	CHR44	43.966	10.7	0.40	29.2	0.0	0.00	23.5	-343.4	-6.83	12.9	4.7
GBR46		47.550	12.2	0.40	26.8	0.0	0.00	24.4	-367.8	-6.83	11.3	5.9
DR20p		47.985	12.4	0.40	26.6	0.0	0.00	24.4	-370.8	-6.83	11.1	6.1
QRR49		50.985	13.6	0.40	26.7	0.0	0.00	23.2	-391.3	-6.83	10.4	7.3
DR21p		51.335	13.7	0.40	26.8	0.0	0.00	23.0	-393.7	-6.83	10.3	7.4
	DR13	54.198	14.8	0.40	28.5	0.0	0.00	20.5	-413.2	-6.83	10.2	8.6
	MER4	54.198	14.8	0.40	28.5	0.0	0.00	20.5	-413.2	-6.83	10.2	8.6
QRR53		54.335	14.9	0.40	28.6	0.0	0.00	20.3	-414.2	-6.83	10.2	8.7
	DR14	54.428	14.9	0.40	28.7	0.0	0.00	20.2	-414.8	-6.83	10.3	8.7
	QLR55	55.428	15.3	0.40	29.6	0.0	0.00	19.1	-421.6	-6.83	11.1	8.6
DR22p		55.498	15.4	0.40	29.7	0.0	0.00	19.0	-422.1	-6.83	11.2	8.5
	DR15	55.595	15.4	0.40	29.8	0.0	0.00	18.9	-422.8	-6.83	11.3	8.4
BZR56		55.798	15.5	0.40	30.0	0.0	0.00	18.7	-424.2	-6.83	11.7	8.3
p-beam	e-beam	Z	Xp	Xp'	12sx	Yp	Yp'	12sy	Xe	Xe'	20sx	20sy
		[m]	[mm]	[mrad]	[mm]	[mm]	[mrad]	[mm]	[mm]	[mrad]	[mm]	[mm]
	CVR56	55.895	15.5	0.40	30.1	0.0	0.00	18.6	-424.8	-6.83	11.8	8.2
DR23p		56.096	15.6	0.40	30.2	0.0	0.00	18.4	-426.2	-6.83	12.2	8.0
BPR57		57.096	15.8	0.00	31.2	0.0	0.00	17.2	-433.0	-6.83	13.8	7.3
DR24p		57.552	15.8	0.00	31.6	0.0	0.00	16.7	-436.1	-6.83	14.6	6.9
QRR59		60.552	15.8	0.00	33.2	0.0	0.00	13.9	-456.6	-6.83	19.6	4.7
	DR16	60.665	15.8	0.00	33.3	0.0	0.00	13.8	-457.4	-6.83	19.8	4.7
DR25p		61.065	15.8	0.00	33.3	0.0	0.00	13.5	-460.1	-6.83	20.3	4.4
MPR4		61.065	15.8	0.00	33.3	0.0	0.00	13.5	-460.1	-6.83	20.3	4.4
DR26p		61.513	15.8	0.00	33.4	0.0	0.00	13.1	-463.2	-6.83	20.2	4.3
	QLR61	61.665	15.8	0.00	33.4	0.0	0.00	13.0	-464.2	-6.83	20.0	4.3
	DR17	61.832	15.8	0.00	33.5	0.0	0.00	12.9	-465.4	-6.83	19.8	4.3
	CVL62	62.132	15.8	0.00	33.5	0.0	0.00	12.7	-467.4	-6.83	19.4	4.3
	DR18	62.531	15.8	0.00	33.5	0.0	0.00	12.4	-470.2	-6.83	18.9	4.3
QRR63		64.513	15.8	0.00	32.8	0.0	0.00	11.2	-485.5	-8.70	16.2	4.4
DR27p		65.365	15.8	0.00	32.4	0.0	0.00	10.8	-493.3	-9.50	15.1	4.5
	BHR64	65.889	15.8	0.00	32.1	0.1	0.25	10.5	-498.4	-10.00	14.5	4.6
	DR19	66.598	15.8	0.00	31.7	0.4	0.58	10.2	-505.5	-10.00	13.6	4.7
	QLR67	67.598	15.8	0.00	31.1	1.2	1.04	9.7	-515.5	-10.00	13.3	4.5
	DR20	68.598	15.8	0.00	30.5	2.4	1.51	9.2	-525.5	-10.00	14.1	4.0
BUR67		69.465	15.8	0.00	30.0	3.9	1.91	8.7				
DR28p		70.155	15.8	0.00	29.7	5.2	1.91	8.4				
BUR72		74.255	15.8	0.00	27.4	17.0	3.83	6.3				
DR29p		74.945	15.8	0.00	27.0	19.7	3.83	6.0				
BUR77		79.045	15.8	0.00	24.7	39.3	5.74	4.0				
DR30p		89.045	15.8	0.00	19.0	96.7	5.74	2.0				

6.2.2 Positrons and Protons

Here we show only the section that exhibits differences to the electron case.

p-beam	e-beam	Z	Xp	Xp'	12sx	Yp	Yp'	12sy	Xe	Xe'	20sx	20sy
		[m]	[mm]	[mrad]	[mm]	[mm]	[mrad]	[mm]	[mm]	[mrad]	[mm]	[mm]
GNL25		-23.800	2.4	-0.56	18.5	0.0	0.00	31.1	-168.4	8.60	19.3	9.7
DL11p		-23.550	2.2	-0.56	18.1	0.0	0.00	31.3	-166.2	8.60	19.5	9.7
GNL23		-21.620	1.1	-0.65	15.3	0.0	0.00	32.3	-149.6	8.60	20.8	10.0
DL10p		-21.370	0.9	-0.65	15.0	0.0	0.00	32.4	-147.5	8.60	21.0	10.1

p-beam	e-beam	Z [m]	Xp [mm]	Xp' [mrad]	12sx [mm]	Yp [mm]	Yp' [mrad]	12sy [mm]	Xe [mm]	Xe' [mrad]	20sx [mm]	20sy [mm]
GNL20		-19.440	-0.5	-0.77	12.8	0.0	0.00	32.2	-130.9	8.60	22.3	10.4
DL9p		-19.200	-0.7	-0.77	12.5	0.0	0.00	32.1	-128.8	8.60	22.4	10.5
BQL19		-18.560	-1.2	-0.97	11.9	0.0	0.00	31.9	-123.3	8.60	22.9	10.6
DL8p		-18.220	-1.5	-0.97	11.5	0.0	0.00	31.7	-120.4	8.60	23.1	10.6
GML17		-14.820	-4.1	-0.56	8.5	0.0	0.00	28.8	-91.2	8.60	25.5	11.3
DL7p		-14.580	-4.3	-0.56	8.3	0.0	0.00	28.5	-89.1	8.60	25.7	11.3
GML13	DL7	-11.180	-5.6	-0.22	6.2	0.0	0.00	22.7	-59.8	8.60	28.2	12.0
ALGM		-10.954	-5.6	-0.22	6.1	0.0	0.00	22.3	-57.9	8.60	28.4	12.0
DLM	ALGM	-10.931	-5.6	-0.22	6.1	0.0	0.00	22.2	-57.7	8.60	28.4	12.0
BOL11	BOL11	-10.431	-5.7	-0.20	5.8	0.0	0.00	21.2	-53.6	8.01	28.7	12.1
DL6	DL6	-10.182	-5.8	-0.20	5.7	0.0	0.00	20.7	-51.6	8.01	28.9	12.2
GJL9	GJL9	-8.302	-6.4	-0.46	4.7	0.0	0.00	17.0	-37.3	7.19	37.4	9.8
DL5	DL5	-7.930	-6.6	-0.46	4.5	0.0	0.00	16.2	-34.6	7.19	40.7	8.8
GIL7	GIL7	-6.050	-7.1	-0.13	3.5	0.0	0.00	12.4	-22.2	5.83	38.3	7.2
DL4	DL4	-5.740	-7.2	-0.13	3.4	0.0	0.00	11.8	-20.4	5.83	34.8	7.5
MPL1	MEL1	-5.740	-7.2	-0.13	3.4	0.0	0.00	11.8	-20.4	5.83	34.8	7.5
DL3	DL3	-5.200	-7.2	-0.13	3.1	0.0	0.00	10.6	-17.2	5.83	28.9	7.9
GOL4	GOL4	-2.000	-7.5	0.00	1.7	0.0	0.00	4.1	-7.5	0.00	7.8	5.0
DL2	DL2	-1.600	-7.5	0.00	1.6	0.0	0.00	3.3	-7.5	0.00	6.4	4.0
MPL0	MEL0	-1.600	-7.5	0.00	1.6	0.0	0.00	3.3	-7.5	0.00	6.4	4.0
DL1	DL1	-0.000	-7.5	0.00	1.3	0.0	0.00	0.4	-7.5	0.00	2.4	0.6
IP	IP	-0.000	-7.5	0.00	1.3	0.0	0.00	0.4	-7.5	0.00	2.4	0.6
DR1	DR1	1.600	-7.5	0.00	1.6	0.0	0.00	3.3	-7.5	0.00	6.4	4.0
MPR0	MER0	1.600	-7.5	0.00	1.6	0.0	0.00	3.3	-7.5	0.00	6.4	4.0
DR2	DR2	1.950	-7.5	0.00	1.7	0.0	0.00	4.0	-7.5	0.00	7.6	4.8
GGR3	GGR3	3.250	-7.5	0.07	2.2	0.0	0.00	6.6	-9.1	-2.43	12.4	8.0
DR3	DR3	3.500	-7.4	0.07	2.3	0.0	0.00	7.1	-9.7	-2.43	13.3	8.6
DR4	DR4	3.852	-7.4	0.07	2.5	0.0	0.00	7.8	-10.5	-2.43	14.6	9.5
GIR5	GIR5	5.732	-7.2	0.12	3.4	0.0	0.00	11.7	-19.3	-6.90	28.7	10.0
DR5	DR5	6.253	-7.1	0.12	3.6	0.0	0.00	12.8	-22.9	-6.90	35.1	8.9
GIR7	GIR7	8.133	-6.7	0.44	4.6	0.0	0.00	16.6	-35.8	-6.73	39.9	9.1
DR6	DR6	8.567	-6.5	0.44	4.8	0.0	0.00	17.5	-38.7	-6.73	36.5	10.0
GJR10	GJR10	10.447	-5.8	0.24	5.8	0.0	0.00	21.2	-53.3	-8.80	29.0	11.8
AABS	AABS	10.692	-5.7	0.24	6.0	0.0	0.00	21.7	-55.4	-8.80	28.8	11.7
EABS	EABS	10.977	-5.7	0.24	6.1	0.0	0.00	22.3	-57.9	-8.80	28.7	11.6
DRM	DRM	11.000	-5.7	0.24	6.1	0.0	0.00	22.3	-58.2	-8.80	28.7	11.5
	MER1	11.000	-5.7	0.24	6.1	0.0	0.00	22.3	-58.2	-8.80	28.7	11.5
p-beam	e-beam	Z [m]	Xp [mm]	Xp' [mrad]	12sx [mm]	Yp [mm]	Yp' [mrad]	12sy [mm]	Xe [mm]	Xe' [mrad]	20sx [mm]	20sy [mm]
ARGM	ARGM	11.180	-5.6	0.24	6.2	0.0	0.00	22.7	-59.7	-8.80	28.6	11.5
GMR13		14.580	-4.2	0.58	8.3	0.0	0.00	28.5	-89.7	-8.80	26.5	10.2
DR7p		14.820	-4.1	0.58	8.5	0.0	0.00	28.8	-91.8	-8.80	26.4	10.1
GMR17		18.220	-1.4	0.99	11.5	0.0	0.00	31.7	-121.7	-8.80	24.4	8.9
DR8p		18.560	-1.1	0.99	11.9	0.0	0.00	31.8	-124.7	-8.80	24.2	8.8
BQR19		19.200	-0.6	0.75	12.5	0.0	0.00	32.1	-130.3	-8.80	23.8	8.6
DR9p		19.440	-0.4	0.75	12.8	0.0	0.00	32.2	-132.4	-8.80	23.7	8.5
GNR20		21.370	1.0	0.64	15.0	0.0	0.00	32.3	-149.4	-8.80	22.6	7.8
DR10p		21.620	1.1	0.64	15.4	0.0	0.00	32.3	-151.6	-8.80	22.4	7.7
GNR23		23.550	2.3	0.55	18.2	0.0	0.00	31.3	-168.6	-8.80	21.4	7.1
DR11p		23.800	2.4	0.55	18.6	0.0	0.00	31.1	-170.8	-8.80	21.3	7.0

6.3 Magnet Positions

In the following tables we give the positions of the magnetic axis, i.e. start point (x_a, z_a) and end point (x_e, z_e), for magnets in the new interaction region.

6.3.1 Magnets seen by the Electron Beam

```
output of HERA-IR spec.code, comp. date: 16/03/00, 09:09
=                  "V4.0,IR_left,e-,920/27.5GeV,0.63/0.26m,M.Seidel,1.2.2000" =
======Name=TName======l==========Za=========Xa=========Ze=========Xe============
     QLL67    QL     2.00000  -67.597933   -0.515500  -66.597983   -0.505500
     BHL64    BH     6.06700  -65.889029   -0.497189  -62.531151   -0.468495
     CVL62    CV     6.76600  -62.132151   -0.466888  -61.832158   -0.464761
     QLL61    QL     7.93300  -61.665163   -0.463576  -60.665188   -0.456487
     CVL56    CV    13.00300  -55.895308   -0.422667  -55.595315   -0.420540
     QLL55    QL    14.17000  -55.428319   -0.419356  -54.428345   -0.412266
     CHL44    CH    24.93300  -43.965607   -0.338084  -43.665615   -0.335957
     QLL43    QL    26.10000  -43.498619   -0.334773  -42.498644   -0.327683
     BNL41    BN    27.86000  -42.238649   -0.326123  -40.738695   -0.314355
     CVL27    CV    41.55100  -27.348192   -0.198906  -27.048203   -0.196326
     BOL11    BO    58.16950  -10.930341   -0.052668  -10.430359   -0.048514
     GJL9     GJ    60.29800  -10.181851   -0.048116   -8.301905   -0.033842
     GIL7     GI    62.55000   -7.929904   -0.032565   -6.049960   -0.018071
     GOL4     GO    66.60000   -5.199981   -0.011120   -2.000008    0.002000
     GGR3     GG    71.85000    1.950000    0.020000    3.250000    0.020000
     GIR5     GI    74.33200    3.852067    0.007263    5.732033   -0.004042
     GIR7     GI    76.73300    6.252957   -0.018488    8.132899   -0.033269
     GJR10    GJ    79.04700    8.566923   -0.032007   10.446863   -0.046998
     CVR27    CV    95.94900   27.048170   -0.199376   27.348158   -0.202016
     BNR41    BN   110.84000   40.738637   -0.320225   42.238591   -0.331946
     QLR43    QL   112.10000   42.498588   -0.333352   43.498565   -0.340181
     CHR44    CH   112.56700   43.665561   -0.341322   43.965554   -0.343370
     QLR55    QL   124.03000   54.428310   -0.414821   55.428287   -0.421649
     CVR56    CV   124.49700   55.595283   -0.422790   55.895276   -0.424839
     QLR61    QL   130.26700   60.665164   -0.457412   61.665141   -0.464241
     CVL62    CV   130.73400   61.832137   -0.465382   62.132130   -0.467430
     BHR64    BH   134.49100   62.531132   -0.468824   65.889013   -0.497079
     QLR67    QL   136.20000   66.597967   -0.505500   67.597917   -0.515500
```

6.3.2 Magnets Seen by the Proton Beam

```
output of HERA-IR spec.code, comp. date: 16/03/00, 09:09
=                  "V4.0IR_left,p_on_e+,920/27.5GeV,2.45/0.18m,M.Seidel,1.2.2000" =
======Name=TName======l==========Za=========Xa=========Ze=========Xe============
     BUL77    BU    14.10000  -79.045233    0.015800  -74.945233    0.015800
     BUL72    BU    18.89000  -74.255269    0.015800  -70.155269    0.015800
     BUL67    BU    23.68000  -69.465277    0.015800  -65.365277    0.015800
     QRL63    QR    27.53200  -64.513277    0.015800  -61.513277    0.015800
     QRL59    QR    31.49300  -60.552277    0.015800  -57.552277    0.015800
     BPL57    BP    32.94900  -57.096277    0.015850  -56.096277    0.015650
     BZL56    BZ    33.54700  -55.798277    0.015481  -55.498277    0.015361
     QRL53    QR    37.71000  -54.335277    0.014896  -51.335278    0.013696
     QRL49    QR    41.06000  -50.985278    0.013556  -47.985278    0.012356
     GBL46    GB    45.34500  -47.550278    0.012182  -43.700278    0.010642
     GBL39    GB    52.45500  -40.440279    0.009338  -36.590279    0.007798
```

```
     GBL34    GB     56.65500    -36.240279    0.007658    -32.390279    0.006118
     GAL30    GA     60.85500    -32.040279    0.005978    -28.190280    0.004438
     BZL28    BZ     61.51500    -27.830280    0.004294    -27.530280    0.004174
     BWL27    BW     62.75500    -26.890280    0.003924    -26.290280    0.003659
     GNL25    GN     65.24500    -25.730278    0.007399    -23.800278    0.006392
     GNL23    GN     67.42500    -23.550277    0.007257    -21.620277    0.006085
     GNL20    GN     69.60500    -21.370276    0.006926    -19.440277    0.005554
     BQL19    BQ     70.48500    -19.200277    0.004358    -18.560277    0.003803
     GML17    GM     74.22500    -18.220287   -0.016044    -14.820287   -0.017372
     GML13    GM     77.86500    -14.580282   -0.016644    -11.180282   -0.016445
     BOL11    BO     78.61450    -10.930391   -0.052667    -10.430409   -0.048514
      GJL9    GJ     80.74300    -10.181893   -0.048116     -8.301947   -0.033842
      GIL7    GI     82.99500     -7.929927   -0.036119     -6.049953   -0.026104
      GOL4    GO     87.04500     -5.200017   -0.011120     -2.000043    0.002000
      GGR3    GG     92.29500      1.950000    0.020000      3.250000    0.020000
      GIR5    GI     94.77700      3.852051    0.000798      5.732029   -0.008328
      GIR7    GI     97.17800      6.252970   -0.022939      8.132930   -0.035160
     GJR10    GJ     99.49200      8.566975   -0.029632     10.446925   -0.043223
     GMR13    GM    103.62500     11.180196   -0.016492     14.580196   -0.016626
     GMR17    GM    107.26500     14.820201   -0.017429     18.220201   -0.016035
     BQR19    BQ    108.24500     18.560191    0.003906     19.200190    0.004464
     GNR20    GN    110.41500     19.440191    0.005653     21.370190    0.006999
     GNR23    GN    112.59500     21.620191    0.006154     23.550191    0.007299
     GNR25    GN    114.77500     23.800192    0.006431     25.730192    0.007412
     BWR27    BW    115.93500     26.290193    0.003662     26.890193    0.003923
     BZR28    BZ    116.87500     27.530193    0.004174     27.830193    0.004294
     GAR30    GA    121.08500     28.190193    0.004438     32.040193    0.005978
     GBR34    GB    125.28500     32.390193    0.006118     36.240193    0.007658
     GBR39    GB    129.48500     36.590193    0.007798     40.440192    0.009338
     GBR46    GB    136.59500     43.700192    0.010642     47.550192    0.012182
     QRR49    QR    140.03000     47.985192    0.012356     50.985192    0.013556
     QRR53    QR    143.38000     51.335191    0.013696     54.335191    0.014896
     BZR56    BZ    144.84300     55.498191    0.015361     55.798191    0.015481
     BPR57    BP    146.14100     56.096191    0.015651     57.096191    0.015851
     QRR59    QR    149.59700     57.552191    0.015801     60.552191    0.015801
     QRR63    QR    153.55800     61.513191    0.015801     64.513191    0.015801
     BUR67    BU    158.51000     65.365191    0.015801     69.465191    0.015801
     BUR72    BU    163.30000     70.155182    0.015801     74.255182    0.015801
     BUR77    BU    168.09000     74.945147    0.015801     79.045147    0.015801
```

6.3.3   Magnets Seen by the Positron Beam

Note the different positions for the GI and GJ magnets as compared to the electron case.

```
output of HERA-IR spec.code, comp. date: 16/03/00, 09:08
=                 "V4.0,IR_left,e+,920/27.5GeV,0.63/0.26m,M.Seidel,1.2.2000" =
======Name=TName======l==========Za=========Xa=========Ze=========Xe===========
     QLL67    QL      2.00000    -67.597977   -0.515500    -66.598027   -0.505500
     BHL64    BH      6.06700    -65.889073   -0.497189    -62.531196   -0.468495
     CVL62    CV      6.76600    -62.132195   -0.466887    -61.832203   -0.464760
     QLL61    QL      7.93300    -61.665207   -0.463576    -60.665232   -0.456486
     CVL56    CV     13.00300    -55.895352   -0.422667    -55.595360   -0.420540
     QLL55    QL     14.17000    -55.428364   -0.419356    -54.428389   -0.412266
     CHL44    CH     24.93300    -43.965652   -0.338084    -43.665660   -0.335957
     QLL43    QL     26.10000    -43.498664   -0.334773    -42.498689   -0.327683
```

BNL41	BN	27.86000	-42.238693	-0.326122	-40.738739	-0.314355
CVL27	CV	41.55100	-27.348237	-0.198906	-27.048248	-0.196326
BOL11	BO	58.16950	-10.930386	-0.052668	-10.430403	-0.048514
GJL9	GJ	60.29800	-10.181895	-0.048116	-8.301950	-0.033842
GIL7	GI	62.55000	-7.929925	-0.036119	-6.049952	-0.026104
GOL4	GO	66.60000	-5.200012	-0.011120	-2.000039	0.002000
GGR3	GG	71.85000	1.950000	0.020000	3.250000	0.020000
GIR5	GI	74.33200	3.852053	0.000798	5.732031	-0.008328
GIR7	GI	76.73300	6.252965	-0.022939	8.132926	-0.035160
GJR10	GJ	79.04700	8.566977	-0.029632	10.446928	-0.043223
CVR27	CV	95.94900	27.048213	-0.199381	27.348201	-0.202021
BNR41	BN	110.84000	40.738680	-0.320230	42.238634	-0.331951
QLR43	QL	112.10000	42.498631	-0.333357	43.498607	-0.340186
CHR44	CH	112.56700	43.665603	-0.341326	43.965596	-0.343375
QLR55	QL	124.03000	54.428352	-0.414823	55.428329	-0.421651
CVR56	CV	124.49700	55.595325	-0.422792	55.895318	-0.424840
QLR61	QL	130.26700	60.665207	-0.457413	61.665184	-0.464241
CVL62	CV	130.73400	61.832180	-0.465382	62.132173	-0.467430
BHR64	BH	134.49100	62.531175	-0.468824	65.889056	-0.497079
QLR67	QL	136.20000	66.598009	-0.505500	67.597959	-0.515500

6.4 Synchrotron Radiation in more Detail

6.4.1 SR Distribution in a Combined Function Magnet

The total synchrotron radiation power from a single electron that is forced to move on a curved trajectory with local radius ρ is given by:

$$
\begin{aligned}
P_\gamma &= \frac{2}{3}\frac{ce^2\beta^4\gamma^4}{\rho^2} \\
&= C_\gamma\frac{cE^4}{2\pi\rho^2}, \quad C_\gamma = 8.8575\cdot 10^{-5}\frac{\text{m}}{\text{GeV}^3}
\end{aligned}
$$

Here γ and β are the relativistic factors for the particle. In a storage ring with circulating beam current I this translates into radiated power per unit length as follows:

$$
\begin{aligned}
\frac{dP_{\text{tot}}}{dl}\left[\frac{\text{kW}}{\text{m}}\right] &= 14.097\,\frac{I[\text{A}]\cdot E^4[\text{GeV}^4]}{\rho^2[\text{m}^2]} \\
&= \frac{C_0}{\rho^2}
\end{aligned}
\tag{14}
$$

The constant C_0 has been introduced to make the expressions below more compact. The direction of the radiated photon is highly collimated in the flight direction of the electron. For simplicity we assume the photon is exactly emitted on the instantaneous trajectory of the electron. Based on the last expression we can now give a formula for the four-dimensional power distribution of the radiation fan from a Gaussianly distributed particle beam:

$$
\frac{dP}{dl}\left(x, x', y, y'\right) =
$$
$$
\frac{C_0}{4\pi^2\varepsilon_x\varepsilon_y}\left\{\left(\frac{1}{\rho}+Kx\right)^2 + K^2y^2\right\}\exp\left(-\frac{\gamma_x x^2+2\alpha_x xx'+\beta_x x'^2}{2\varepsilon_x}\right)\exp\left(-\frac{\gamma_y y^2+2\alpha_y yy'+\beta_y y'^2}{2\varepsilon_y}\right)
$$

We assume here a combined function magnet that deflects the beam horizontally with bend radius ρ and k-value K. ε_x and ε_y are the horizontal and vertical emittance of the particle beam. Above expression is valid only for a thin longitudinal slice of the magnet. The optical functions $\beta_{x,y}$, $\alpha_{x,y}$ and $\gamma_{x,y}$ are functions of the longitudinal position. We use the original notation from Courant and Snyder [18], where $\alpha = -\beta'/2$ and $\gamma = (1+\alpha^2)/\beta$ (this γ, β should not be confused with the relativistic factors). In a standard situation one is interested in the projected power distribution of the radiation, some distance away from the magnet. This is obtained by the following coordinate transformation and an integration over all angles:

$$x = x_1 - \Delta z x', \; x' = x_1', \; y = y_1 - \Delta z y', \; y' = y_1'$$

$$
\begin{aligned}
\frac{dP}{dl}(x_1, y_1) &= \int_{-\infty}^{\infty} dx_1' \int_{-\infty}^{\infty} dy_1' \frac{dP}{dl}(x_1, x_1', y_1, y_1') \\
&= \frac{C_0}{2\pi\sqrt{\varepsilon_x \beta_x^s \varepsilon_y \beta_y^s}} \left[\frac{\varepsilon_x \Delta z^2 K^2}{\beta_x^s} + \left(\frac{1}{\rho} + x_1 K \frac{\beta_x^s + \alpha_x^s \Delta z}{\beta_x^s} \right)^2 + \dots \right. \\
&\quad \left. \dots \frac{\varepsilon_y \Delta z^2 K^2}{\beta_y^s} + y_1^2 K^2 \left(\frac{\beta_y^s + \alpha_y^s \Delta z}{\beta_y^s} \right)^2 \right] \exp\left(-\frac{x_1^2}{2\varepsilon_x \beta_x^s} \right) \exp\left(-\frac{y_1^2}{2\varepsilon_y \beta_y^s} \right) (15)
\end{aligned}
$$

Here Δz is the distance from the point where the radiation is originated to the observation plane, the new coordinates are x_1, x_1', y_1, y_1', furthermore we use optical functions with superscript s for the photon beam at the observation plane:

$$\beta^s = \gamma \Delta z^2 - 2\alpha \Delta z + \beta, \;\; \alpha^s = \alpha - \gamma \Delta z \tag{16}$$

The horizontally projected distribution is obtained by an integration over y_1:

$$
\frac{dP}{dl}(x_1) = \frac{C_0}{\sqrt{2\pi \varepsilon_x \beta_x^s}} \left[\frac{\varepsilon_x \Delta z^2 K^2}{\beta_x^s} + \left(\frac{1}{\rho} + x_1 K \frac{\beta_x^s + \alpha_x^s \Delta z}{\beta_x^s} \right)^2 + \beta_y \varepsilon_y K^2 \right] \exp\left(-\frac{x_1^2}{2\varepsilon_x \beta_x^s} \right)
$$

Finally we obtain the total radiated power by performing the last integration over x_1:

$$\frac{dP}{dl} = C_0 \left[\frac{1}{\rho^2} + K^2 (\beta_x \varepsilon_x + \beta_y \varepsilon_y) \right] \tag{17}$$

Here we can clearly distinguish the contributions to the power produced by the dipole and quadrupole parts of the magnetic field.

6.4.2 Selected Radiation Patterns

In this section we show SR power density distributions, computed with the above algorithms, for selected locations in the IR (all obstacles, beampipes etc. are neglected).
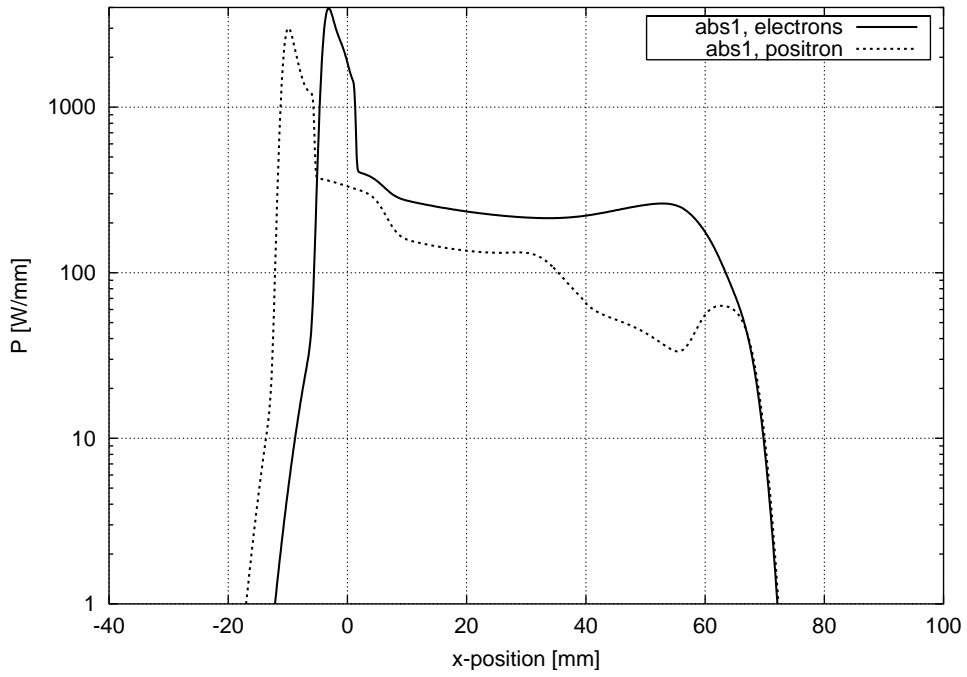
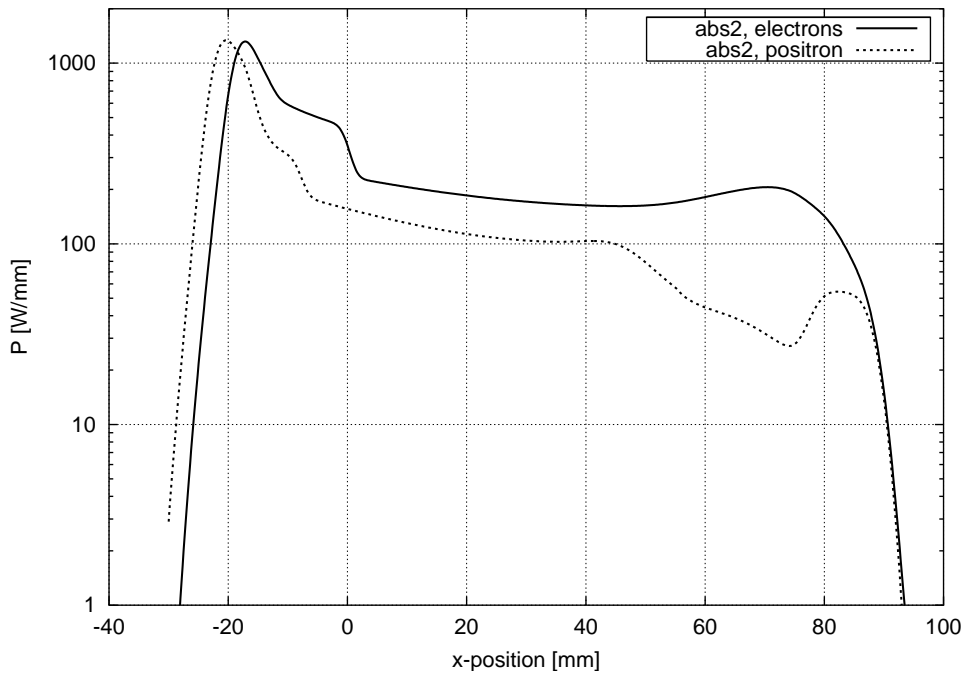Figure 18: Horizontal line density at Absorber 1.

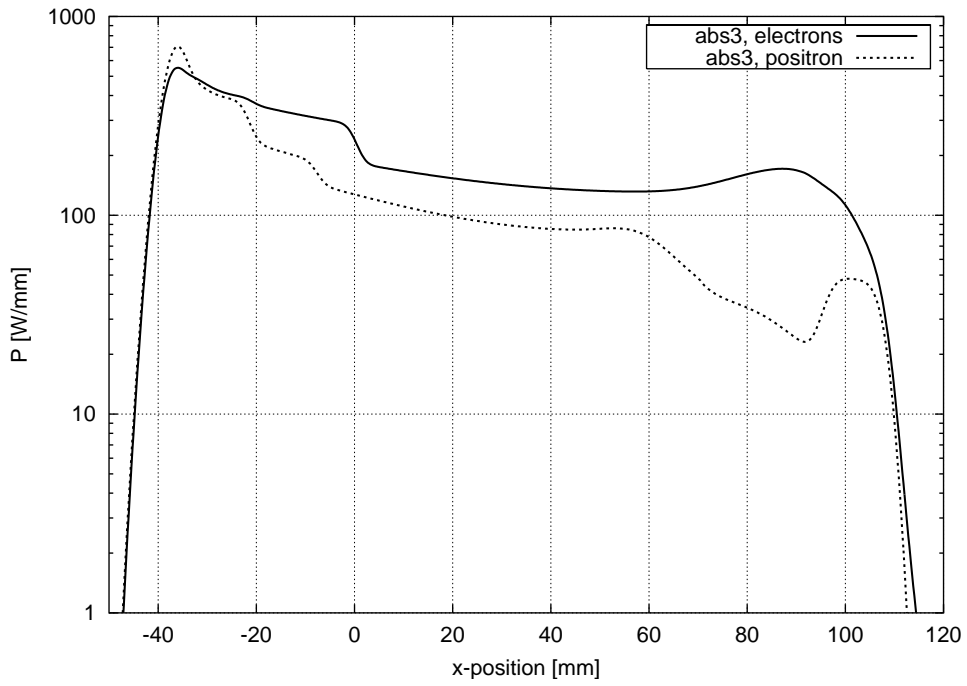Figure 19: Horizontal line density at Absorber 2.

Figure 20: Horizontal line density at Absorber 3.
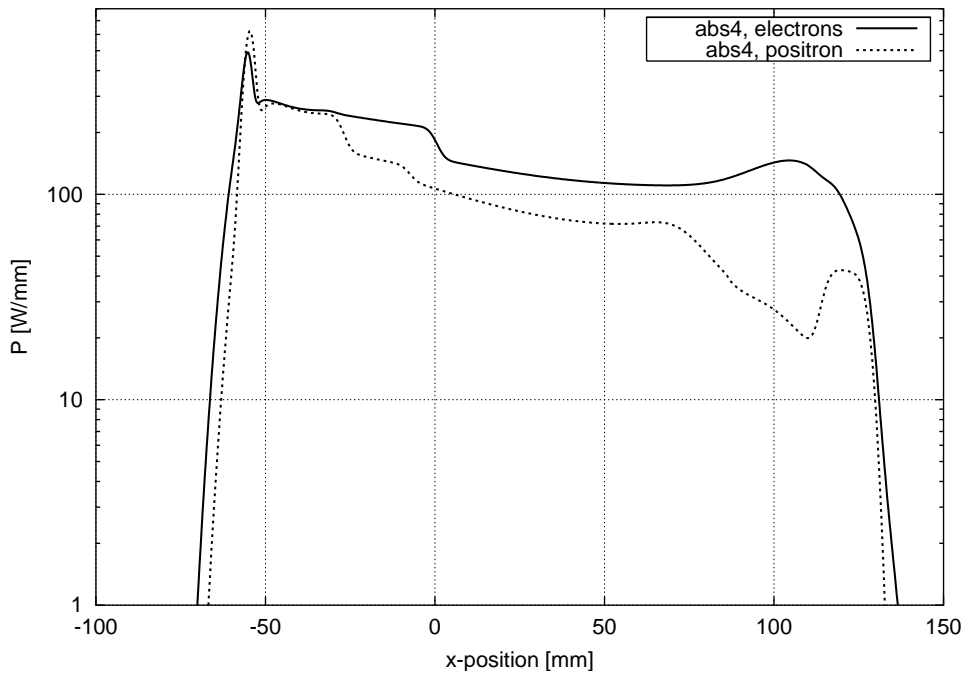

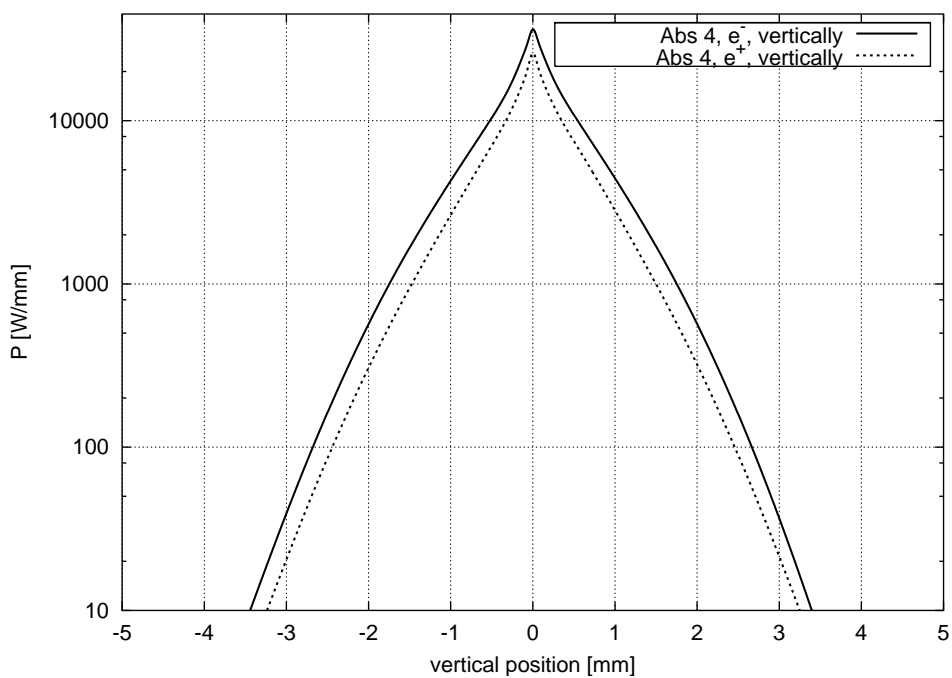Figure 21: Horizontal line density at Absorber 4.
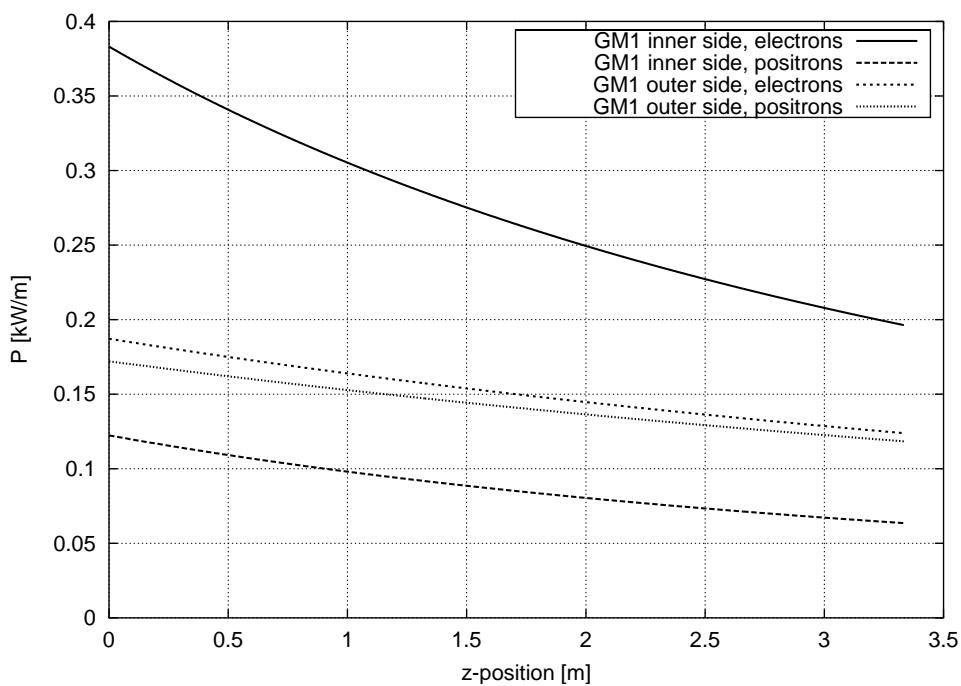
Figure 22: Vertical line density at Absorber 4.

Figure 23: Horizontal line density in the first GM chamber (proton pipe, z-scale starting at magnet entrance).
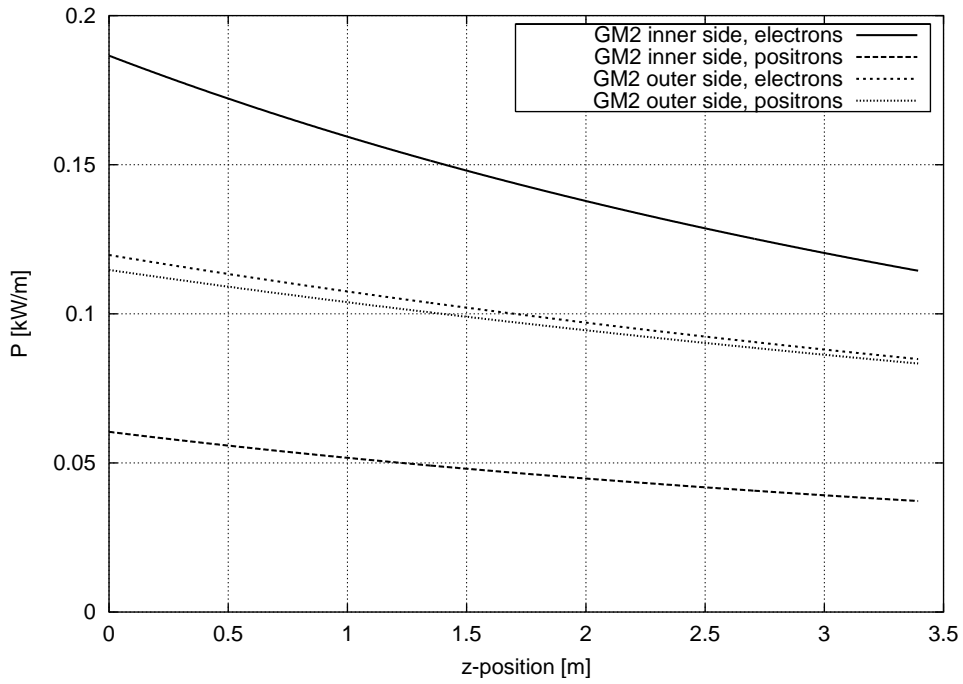
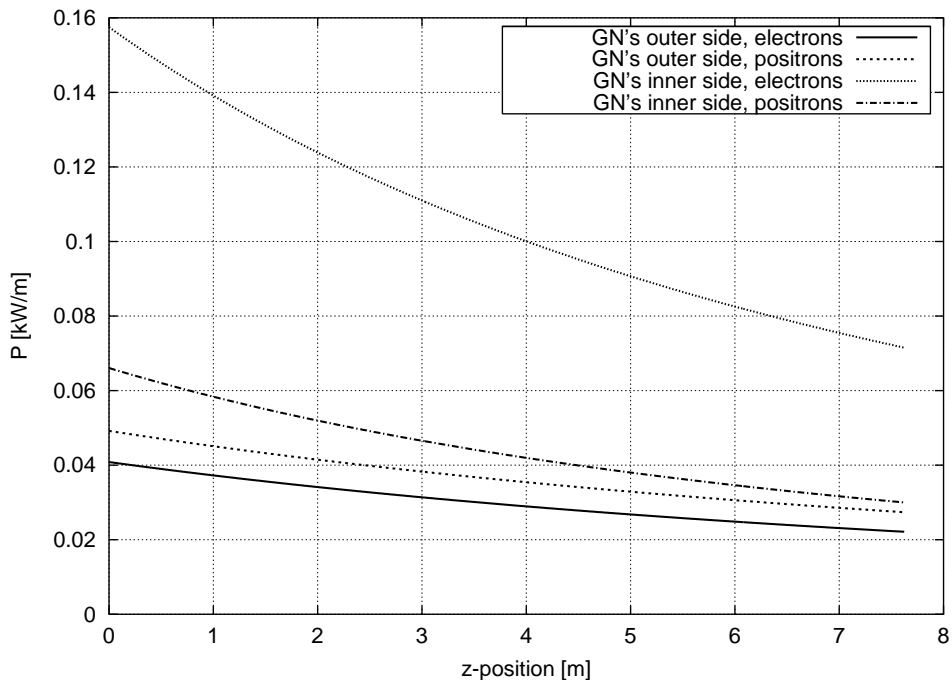Figure 24: Horizontal line density in the second GM chamber (proton pipe).

Figure 25: Horizontal line density in the three GN chambers (proton pipe, z scale starts at entrance of first GN at 19.44 m).
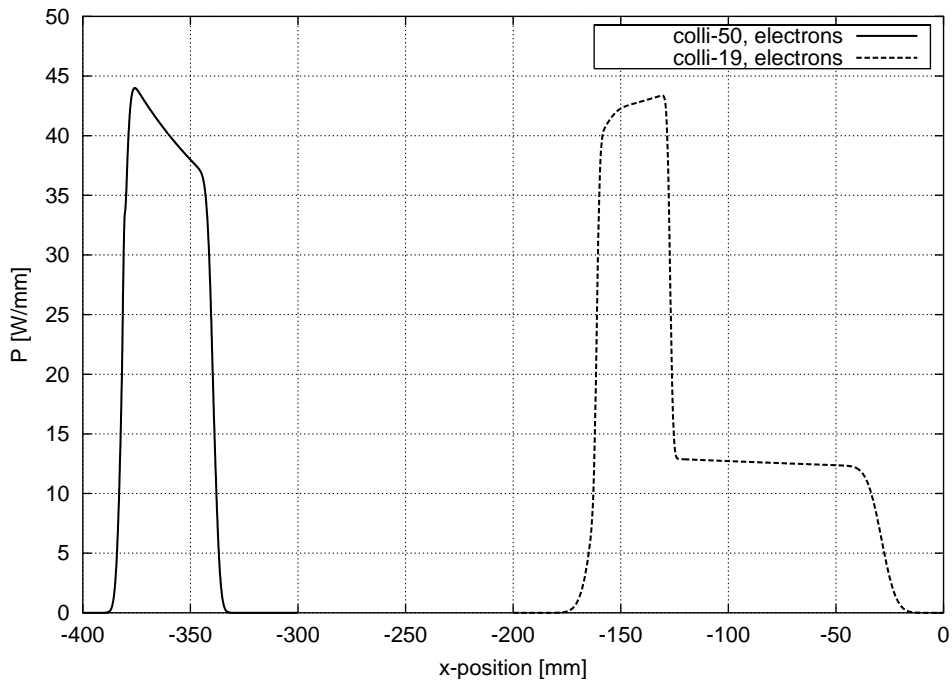
Figure 26: Horizontal line density at the SR collimators 19 m and 50 m left. The patterns for positron operation are identical.
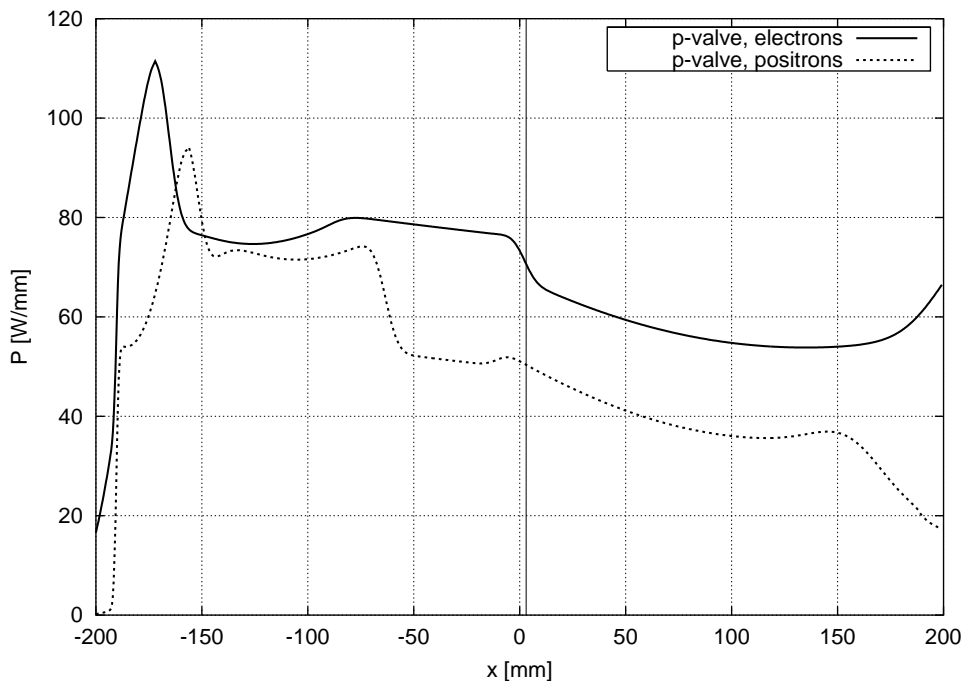

Figure 27: Horizontal line density at the proton vacuum valve, 26 m right. The line indicates the proton beam position.

References

[1] F. Willeke, HERA status and upgrade plans, DESY-M-97-10s, or PAC97, Vancouver (1997) 1

[2] U. Schneekloth (Ed.), The HERA Luminosity Upgrade, DESY internal report (1998) 1

[3] B. Holzer, e.g. Meeting on HERA Luminosity Upgrade Nr. 83, 91, minutes (1999, 2000) 2

[4] G. Hoffstätter, HERA Seminar Grömitz (1999), or PAC99, New York (1999) 2

[5] M. Berglund, doctoral thesis to be published, or Meeting on HERA Luminosity Upgrade Nr. 82, 92, minutes (1999, 2000) 3, 19

[6] E. Lohrmann, Synchrotron Radiation at the ZEUS Interaction Region after Luminosity Upgrade, ZEUS note 00-2 (2000) 11

[7] U. Kötz, Meeting on HERA Luminosity Upgrade Nrs. 30 and 67, minutes (1998, 1999) 11

[8] M. Bieler et al., Design of a high power synchrotron radiation absorber for HERA, PAC 99, New York (1999) 13

[9] J. D. Jackson, Classical Electrodynamics, Wiley & Sons (1975) 16

[10] E. Lohrmann, Meeting on HERA Luminosity Upgrade, Nr. 71, minutes (1999) 17

[11] K. Wittenburg, Some Thoughts Concerning the SR Monitor at 24 m for the HERA Upgrade, DESY internal note MDI 99-03 (1999) 17

[12] K. Wittenburg, Some New Thoughts Concerning the SR Monitor at 95 m for the HERA Upgrade, DESY internal note MDI 99-04 (1999) 17

[13] Ch. Montag, Meeting on HERA Luminosity Upgrade, Nr's. 30, 71, 78, minutes (1998, 1999) 19

[14] E. Gianfelice, Meeting on HERA Luminosity Upgrade, Nr. 30, minutes (1998) 19

[15] W.H. Press et al., Numerical Recipes in C, Cambridge University Press (1992) 21

[16] G. White, T. Himel and H. Shoaee, A Hybrid Numerical Method for Orbit Correction, SLAC-Pub 7653 (1997) 22

[17] F. Stulle, Einfluß externer Sörungen auf die Stabilität des Wechselwirkungspunktes in HERA, diploma thesis under work 23

[18] E.D. Courant and H.S. Snyder, Theory of Alternating-Gradient Synchrotrons, Annals of Physics 3, 1 (1958) 33

The HERA upgrade meeting minutes can be found on the WWW under http://pia.desy.de. Login as **guest** is possible without password.